Printing path-dependent two-scale models for 3D printed planar auxetics by material extrusion

Bol, Rowin J.M.; Xu, Yading; Šavija, Branko

DOI
10.1016/j.addma.2024.104293

Publication date
2024

Document Version
Final published version

Published in
Additive Manufacturing

Additive Manufacturing 89 (2024) 104293

Contents lists available at ScienceDirect

Additive Manufacturing

journal homepage: www.elsevier.com/locate/addma

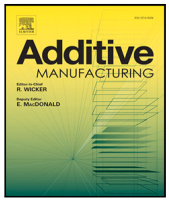

Research Paper

Printing path-dependent two-scale models for 3D printed planar auxetics by material extrusion

Rowin J.M. Bol *, Yading Xu, Branko Šavija

Microlab, Faculty of Civil Engineering and Geosciences, Delft University of Technology, Stevinweg 1, 2628 CN Delft, The Netherlands

ARTICLE INFO

Keywords:
Auxetics
Additive manufacturing (AM)
Material extrusion
Mechanical anisotropy
Two-scale modelling
Lattice beam model (LBM)

ABSTRACT

One particularly interesting class of mechanical metamaterials are those having a negative Poisson's ratio, which are referred to as 'auxetics'. Because of their geometrical complexity, auxetic designs cannot always be easily created. However, Additive Manufacturing (AM) methods like material extrusion in 3D printing present the opportunity to construct auxetic structures. Nevertheless, extruded 3D printed material can be highly anisotropic. Before 3D printed auxetics manufactured through material extrusion can be used in engineering applications, it is important to generate powerful simulation tools that can reliably reproduce and foretell their mechanical characteristics irrespective of their form and intricacy. In view of this, the current work proposes printing path-dependent models based on an experimentally validated multi-scale modelling scheme using the Lattice Beam Model (LBM). This is done by first representing idealized microstructures of extruded 3D printed polymers through geometric models and simulating these on the material scale. The aim is to explicitly model the inter-layer and intra-layer bonds that exist in material extruded 3D printed parts by assigning experimentally obtained interface properties that significantly differ from the bulk material. On the auxetic structure scale, two planar auxetic designs are modelled using the determined material scale relationships as input: Re-Entrant (RE) and Rotating Square (RS). In terms of mechanical response, the experimentally and numerically obtained force displacement curves agree reasonably well: the stiffness of the modelled auxetic designs fit well with the experimentally measured ones while the LBM simulations generally provide a good estimation in strength. Finally, it has been shown on both the material and auxetic structure scales that incorporation of the interfacial bond strengths in simulations of extruded 3D printed polymers is important, because neglecting these results in significant overestimation of the strength.

1. Introduction

In view of recent advances in Additive Manufacturing (AM) techniques, mechanical metamaterials have emerged [1] that exhibit extraordinary properties because of their rational designs [2]. Metamaterials can be defined as man-made materials having properties that are unseen in natural materials [3]. One particularly interesting class of mechanical metamaterials are those having a negative Poisson's ratio, which are referred to as 'auxetic materials' [4–17]. Auxetic materials are known to have a variety of mechanical properties that are scarce in common natural (non-auxetic) materials: synclastic curvature in bending, variable permeability, high shear stiffness, high specific strength, enhanced indentation resistance, high fracture toughness, impact resistance, fatigue toughness, improved damping, sound and energy absorption properties, and being lightweight [3,7–9,11,14–21]. Because of their geometrical complexity, auxetic designs cannot always be easily created [6]. However, AM methods like 3D printing present the opportunity to construct auxetic structures, as suggested in the latter reference. Nevertheless, AM techniques are prone to several issues that affect the auxetic behaviour. For example, 3D printed material can be highly anisotropic [8]. AM parts can also contain various geometrical imperfections [13], while it is important to have sufficient printing accuracy in relation to mechanical properties of auxetic designs [6,22].

It is known that a material's auxetic response and its related mechanical characteristics strongly depend on the deformation mechanism [11]. Based on these deformation mechanisms, auxetic materials can be classified. Numerous designs exist that (potentially) possess auxetic behaviour of which the most common and important classes are honeycomb arrangements of re-entrant models [3–8,11–14,22–26], rotation unit mechanisms [3,4,8,11,12,15,22] and chiral mechanisms [3,8,11,12,15,22,25,26]. Some auxetic designs may have a varying Poisson's ratio under deformation as a result of their structural motif, like re-entrant mechanisms. Other classes may only exhibit auxetic

* Corresponding author.
E-mail address: R.J.M.Bol@tudelft.nl (R.J.M. Bol).

https://doi.org/10.1016/j.addma.2024.104293
Received 9 February 2024; Received in revised form 3 May 2024; Accepted 2 July 2024
Available online 14 July 2024

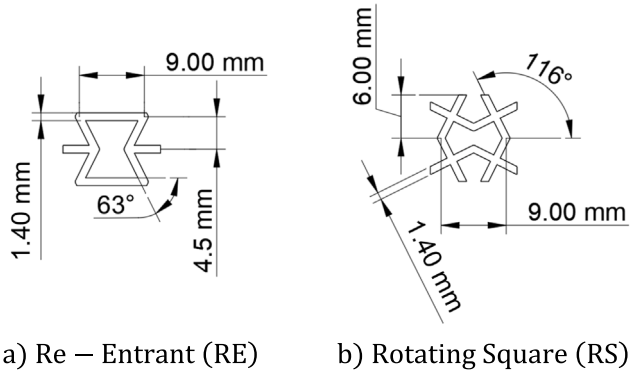

Fig. 1. Design parameters for (a) Re-Entrant (RE) and (b) Rotating Square (RS) auxetic structures (unit cells).

behaviour under compression, such as buckling induced mechanisms, while different ones only work in tension, which is the case for fibril/nodule mechanisms [11]. It is therefore essential to gain a thorough comprehension of the different deformation mechanisms involved in auxetic structures when selecting, designing and using auxetic materials for engineering applications.

Because of their enhanced mechanical characteristics, auxetic materials already have applications in numerous fields, such as automotive [6–8,15,27], aerospace [6,8,14,15], military [6,7,15], (bio)medical [6,7,11–15,20,27], textile industry [7,11], construction industry [11, 15,20,21], and protection [6,11,14]. Some examples of applications in the aforementioned fields are biomedical stents [12,25], military and protection knee caps, safety jackets and helmets [6,11], fastener, rivets and sandwich panels in construction [11,20,21], and fiber-reinforced composites [11,20]. Future extensions may include specific engineering applications, like impact resistance structures and vibration mitigation structures [16], for instance in barriers for offshore break-waters and earthquakes in extreme conditions [17], respectively.

Recently, several studies have been performed that the use of 3D printed polymeric lattice reinforcement can improve the properties of cementitious composites [28–30]. Among these, auxetic designs have shown the best performance when the composite is subjected to uniaxial compression [31]. Nevertheless, the fabrication procedure of these reinforcements has a great influence on their mechanical behaviour, which is strongly dependent on the printing and loading directions [32]. In this study, therefore, we chose to focus on print-path dependent modelling of the two auxetic designs that showed the best performance in our previous work, namely Re-Entrant (RE) and Rotating Square (RS) [31].

RE is the most basic and widely studied class of auxetic materials [3–8,11–14,22–26]. These auxetic structures typically consist of thin ribs or trusses that are connected by hinges. The result is a polygonal truss having a repetitive pattern, usually referred to as a unit cell [11]. The term refers to one polygon angle being larger than 180° or negative [7]. One famous design is the RE bowtie honeycomb structure, whose unit cell is shown in Fig. 1(a). RS is sometimes distinguished as another auxetic model in literature (e.g. [4]), referred to as a type of missing rib mechanism. Fig. 1(b) depicts its unit cell. This specific auxetic design gets classified under most deformation mechanisms in various other literature (e.g. [4,12,22]). However, because of its rotational deformation mechanism, in this work it will be referred to as RS, similar to the former study by Xu & Šavija [31].

A review on micromechanical models for extruded 3D printed polymers, specifically Fused Deposition Modelling (FDM), is provided in a previous work by Bol & Šavija [33]. Therein, we conclude that incorporating the (large) anisotropy present within microstructures of 3D printed parts manufactured through FDM needs more dedication to this day. Before 3D printed auxetics manufactured through material extrusion can be used in engineering applications, it is important to generate powerful simulation tools that can reliably reproduce and foretell their mechanical characteristics irrespective of their form and intricacy. One example are the printing paths, which can be straight but frequently alternate their course already in one layer. Especially for these deviating instances, it is important that material properties get allotted corresponding to all different printing path directions. Albeit Monaldo & Marfia [34] were the first to suggest a two-scale methodology for extruded 3D printed polymers which models microstructural geometries that consider both the voids and pores as well as the inter-layer and intra-layer bond strengths, an important development in this research area, it remains limited to constant printing paths within one layer. If printing paths are frequently alternating (already in the same layer), so is the directionality of the interfacial bonds which imposes supplementary directional-dependent anisotropy or *printing path-dependent anisotropy*. Put differently, printing path-dependent models are required that incorporate the characteristic features of extruded 3D printed polymers' microstructures.

In view of this, the current work proposes printing path-dependent models based on an experimentally validated two-scale modelling scheme using the Lattice Beam Model (LBM). This is done by first representing idealized microstructures of 3D printed polymers through geometric models described in [33] and simulating these on the material scale. The aim here is to explicitly model the inter-layer and intra-layer bonds by assigning experimentally obtained interface properties that significantly differ from the bulk material. To the authors' knowledge, this is the first time experimentally obtained inter-layer bond and intra-layer bond properties are explicitly considered in numerical simulations of 3D printed parts by material extrusion. On the auxetic structure scale, planar auxetic designs are modelled using the determined material scale relationships as input. In this approach, printing path directions can be straightforwardly received through the 3D printer's G-code containing all information about printing temperature, printing speed, nozzle size, layer thickness and motions for extruding the polymer material. The allocation of printing path-dependent material characteristics is executed by coupling the printing path directions to a locally introduced coordinate system wherein the main axis follows the printing path while the other two reflect the interfacial bond properties. The resulting simulation tools present a powerful, factual and trustworthy numerical methodology for extruded 3D printed polymers as these incorporate the mechanical characteristics of both interfacial bond strengths due to the AM technique of material extrusion.

2. Modelling of deformation & fracture

Schlangen and van Mier suggested a numerical approach for simulating fracture in concrete in the 1990s, known as lattice modelling [35, 36]. The lattice concept was adopted from the field of theoretical physics [35,37] and was first used to study elasticity problems of continua by Hrennikoff [38] in the 1940s. In this discrete approach the material is discretized into a lattice of two-node elements that transfer the forces [39]. These can be springs [40,41], but usually trusses or beams are used as it has been shown that the latter provides more accuracy on fracture patterns [42]. Lattice models enable to study and take the material's microstructure into consideration [43] through superimposing the lattice network over original (micro)structures [36]. Heterogeneity can be incorporated by implementing an irregular mesh or assigning different material characteristics to each element [44] and fracture is included through element removal, sometimes preceded by (gradual [45]) stiffness deterioration [46].

LBM has proved to be successful in simulating fracture for various types of material besides concrete, e.g. cement-paste, (porous reactor core) graphite and wood, as addressed in [32,39,47–50]. It has also been applied to simulate fracture processes of steel reinforced and

fiber reinforced cementitious materials [51] and structural behaviour of reinforced concrete at the macroscale [52,53], including interface modelling of ribbed re-bars [50]. So, the approach has been used to model concrete at various length-scales (micro-, meso- and macro-scale) [52]. Furthermore, the model has also been used for purposes other than fracture, such as moisture transport and chloride diffusion in cement-based systems [53,54]. More recent applications of LBM can be found in the field of AM for 3D Concrete Printing (3DCP) by Chang [55–58].

In terms of models for FDM 3D printed plastics, numerous efforts have been made through a variety of (microstructural) modelling strategies in literature [33]. Given the promising implementations of LBM for multi-phase particulate materials, like concrete [36,41] with its different phases (e.g. aggregates, cementitious matrix and interface [43] or ITZ [59]), it is believed that the inter-layer and intra-layer bonds that exist in FDM 3D printed parts can be modelled explicitly using LBM. Variations in element properties as a result of processing techniques like FDM can be simply incorporated through assigning different input properties to each lattice element [3]. The model has already been used for FDM 3D printed lattice materials by Xu et al. [32] in which the anisotropy as a result of the FDM method was only *implicitly* incorporated in the model, i.e. by adjusting the constitutive law of beam elements, resulting in accurate predictions of the material's fracture behaviour and mechanical response in uniaxial tensile tests. Additionally, imperfections (caused by the FDM process) can be easily incorporated in the LBM [55] by means of superimposing.

2.1. Lattice beam model

The basis of LBM is to discretize a material into a network of beam elements that are connected at their ends [45,53]. Since in this case the ratio between the length and cross-sectional dimensions of these beam elements is small, Timoshenko beam elements are used to account for shear deformation [48,58,60]. These elements are assigned certain material properties [53], which are generally linear-elastic (e.g. [45,50,51]) but can also be non-linear (e.g. [39,52,61]). Although the locally assigned behaviour of an element may be brittle, a global quasi-brittle or ductile response can be obtained [45,49,50]. Fracture is simulated through loading the lattice by a prescribed deformation or an imposed load, followed by carrying out a linear elastic analysis. Subsequently, the stresses occurring in each element are compared to a prescribed failure criterion (e.g. strength, strain, or energy criteria can be used [50]). An element that exceeds this criterion is removed from the mesh, thereby representing a micro-crack (i.e. fracture) in the material. The reaction forces and displacement field are stored in each analysis step and the procedure is repeated: the damaged lattice is reloaded, discarding one element at a time until the network of beam elements ultimately fails. This stepwise removal procedure basically mimics crack initiation and propagation. In this way, all performed linear-elastic analyses form one non-linear analysis by which realistic crack patterns can be obtained [45,50]. For details of the method, e.g. its solution procedure or stiffness matrix assemblies, the reader is referred to the works of Qian [35,36].

2.2. Lattice generation

The method for lattice generation presented here generally follows the procedure as described in [3,32,45,51]. The part to be modelled is discretized into a grid of cubic cells (3D lattice) or square cells (2D lattice [45]), as shown in Fig. 2 for simplicity. Within every cell, having length A, sub-cells are generated with length s such that $0 \leq s \leq A$. Inside these sub-cells, lattice nodes are randomly positioned. This randomness is defined as the ratio between the sub-cell size s and cell length A:

$$R = \frac{s}{A}\,. \tag{1}$$

Disorder in the lattice mesh is introduced through population of a single lattice node inside each sub-cell based on random seeds obtained from a list of generated pseudo random numbers. Therefore, heterogeneity is already built-in. R is set to 0.5 in this study. In the case of a 3D analysis, all nodes have six degrees of freedom (three translations and three rotations) [45]. The method for lattice network generation will be explained next. The starting point is similar to the heterogeneous rectangular or quadrangular lattice network constructions used in e.g. [36,51], where quadrangular meshes are used that simply connect the lattice nodes parallel to the three main directions (i.e. along the X, Y and Z axes) without any diagonals. However, the lattice network generation method adopted here considers all adjacent directional connectivity possibilities. Besides the three main directions (XX, YY and ZZ), it also considers planar diagonals (XY, YZ and XZ) and spatial diagonals (XYZ). It should be noted that this holds for any lattice node, meaning that duplicate and intersecting beam elements are unavoidable without any measures. To this end, certain criteria are enforced during the lattice network construction. Planar diagonals in each direction (XY, YZ and XZ) have two possible orthogonal configurations. Without any criterion, both orthogonal configurations would be generated causing intersections. This is avoided by measuring the length of both elements and only selecting the shortest one for all neighbouring lattice nodes in each planar diagonal direction. The same procedure is adopted for the spatial diagonals (XYZ) having four possible mutually orthogonal configurations.

The phase to which each beam element belongs is identified through superimposing the lattice onto a geometrical representation of the part to be modelled, including its material composition. For instance, the domain in Fig. 2 represents the microstructure of an FDM 3D printed polymer and contains four quarters of elliptical filaments, referred to as bead regions (the bulk material), and a central void region. If the two end nodes of a beam element are both located in the same bead region (i.e. one of the four quarters), it is defined as an element belonging to the bead phase and assigned its corresponding material properties. In the case of Fig. 2, when the two end nodes are located in different vertically adjoining bead regions, the element is considered as an inter-layer element. Similarly, if the two end nodes are positioned in different horizontally neighbouring bead regions, the beam element receives intra-layer properties (see Fig. 2). Lattice nodes that appear inside a void region are excluded from the mesh, including the elements that would be connected these nodes (indicated by the grey dashed lines in Fig. 2).

2.3. Failure analysis

The stresses occurring in each beam element are determined as follows [3,32,50,55,58,60,62]:

$$\sigma = \alpha_{\mathrm{N}} \frac{N}{A} + \alpha_{\mathrm{M}} \frac{\max\left(|M_i|, |M_j|\right)}{W}\,, \tag{2}$$

where N is the normal force in the lattice element, A the cross-sectional area, M_i and M_j are the local bending moments in nodes i and j, W is the section modulus, α_{N} and α_{M} are the normal force and bending moment influence factors, respectively. Based on the aforementioned studies, α_{N} and α_{M} are taken as 1.0 and 0.05, respectively. The failure criterion used in the simulations presented here is based on strength, i.e. stress ($\mathbb{F}(\sigma)$):

$$\mathbb{F}(\sigma) = \frac{\sigma}{f_{\mathrm{y}}} \leq 1\,, \tag{3}$$

where σ is the stress computed using Eq. (2) and f_{y} the material's strength. If exactly one element reaches this failure criterion, i.e. $\mathbb{F}(\sigma) = 1$, the element is considered to have failed which results in removal from the mesh as stressed before.

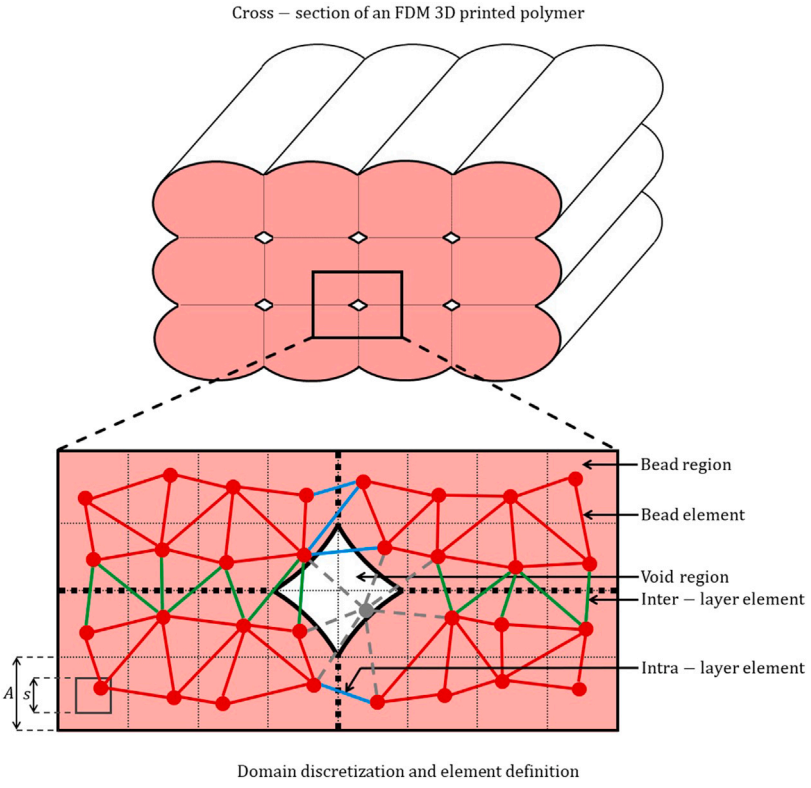

Fig. 2. Schematics of domain discretization and element definition (shown in 2D for simplicity).

3. Methodology

In the experimentally validated two-scale modelling scheme proposed here, constitutive relationships of lattice beam elements are derived from material scale (i.e. microstructural) simulations, providing input for local lattice elements in auxetic structure scale models [60]. Similar approaches using LBM have been previously described and found to be successful in various literature [36,39,49,61,63]. Numerical simulations of deformation and fracture using fine meshes for the microstructural model are computationally expensive [39], especially when a single length-scale approach is used this could be even impossible [49,61]. To this end, the auxetic structure scale is discretized into smaller cubic cells. Subsequently, numerical simulations of tensile tests are performed on these smaller cubic cells, so-called material scale simulations. As a result of the material scale simulations, load–displacement and stress–strain curves are obtained that are schematized as multi-linear constitutive relationships to be used for the beam elements in the auxetic structure scale simulations. The beam elements are assigned with multi-linear relations obtained at the material scale, see Fig. 3. Therefore, elements are not immediately removed in each analysis step, but their stiffness and strength change according to the implemented constitutive relationship. Once the element reaches its initial maximum stress, this element will adopt the stiffness and strength of the following point on the multi-linear curve. The element is only considered to have fully failed past the final point, which results in removal from the mesh as explained previously.

The first step in the two-scale modelling strategy is to geometrically describe and idealize the microstructures of extruded 3D printed material using the microstructural models established in [33]. The resulting geometric model will be used as input for the LBM simulations as discussed in Section 2.1. Similar to what is often done in Finite Element Analysis (FEA), the general aim here is to determine a Representative Volume Element (RVE). However, besides the general approach to represent the microstructural morphology with the internal porosity,

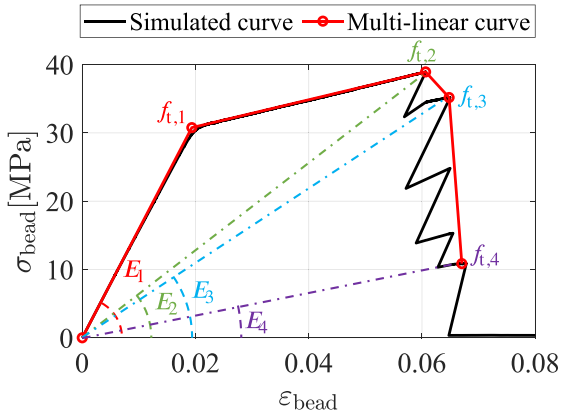

Fig. 3. Example of a multi-linear constitutive relationship obtained at the material scale.

which is already often done in literature, this study aims to explicitly model the interfacial bonds by assigning experimentally obtained interface properties that significantly differ from the bulk material.

To incorporate the effects of both porosity and internal bonds, the following methodology is proposed here. Initially, constitutive relationships shall be determined experimentally for three distinguished phases, namely: (i) the bead or filament phase (i.e. the 'bulk material' without interfaces), (ii) the inter-layer bond phase, and (iii) the intra-layer bond phase. Their respective relationships will be obtained from material scale uniaxial tensile tests on dog bone shaped specimens. Seeing the significant consequences of (minor deviations in) printing settings on the material behaviour of 3D printed polymers [33], these are kept constant throughout all length scales. Afterwards, the RVE will be modelled by means of LBM simulations using the measured geometrical input and constitutive relationships, thereby explicitly incorporating the effects of both porosity and internal bonds. Finally, the

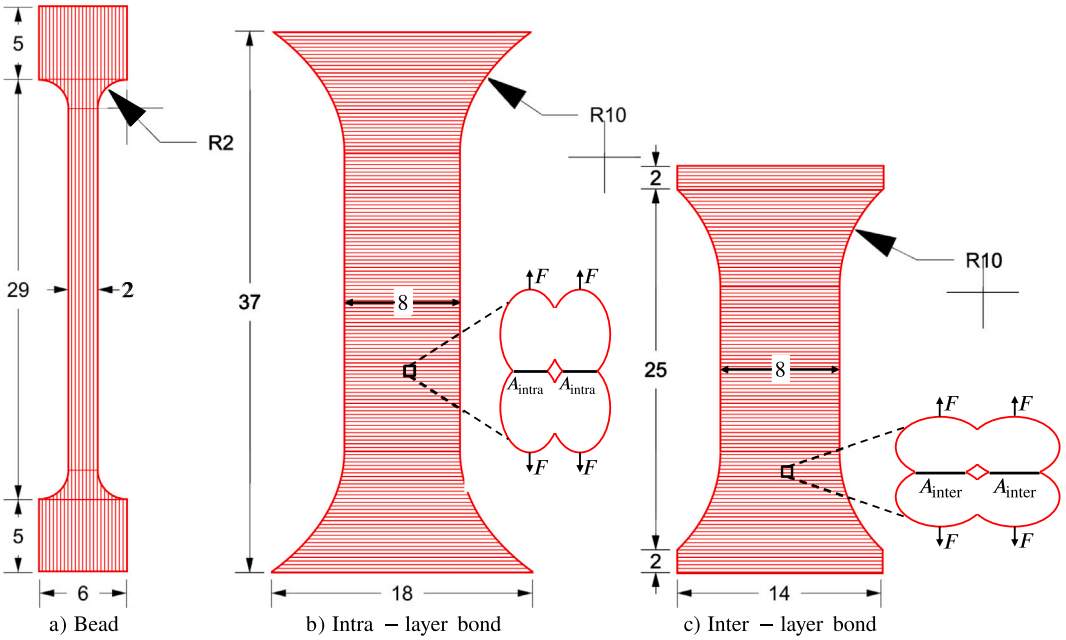

Fig. 4. Schematics of material scale dog bone shaped specimens for (a) bead, (b) intra-layer bond, and (c) inter-layer bond property determination (dimensions in mm).

approach will be validated by means of auxetic structure scale LBM analyses of the planar auxetic designs using the determined material scale relationships as input.

3.1. Microstructural experimental analysis

Failure of extruded 3D printed polymers mainly occurs along layer interfaces [33,64], which is mainly due to poor attachment among layers, and must therefore be explicitly modelled. Occasionally, the tensile strength of parts that are printed in the vertical direction is utilized to estimate this interfacial strength [65]. Nonetheless, oftentimes it is not possible to acquire the interfacial strength among layers straightforwardly through stress and strain data [66,67]. Therefore, this study will use material scale dog bone shaped specimens to obtain interface strengths to be used as input for the LBM simulations. Three different kinds of specimens have been designed to experimentally determine the constitutive relationships for the bead, inter-layer bond and intra-layer bond phases of the RVE, respectively. Acrylonitrile Butadiene Styrene (ABS) is used as polymer filament, similar to [28]. Starting with the bead phase, which can be regarded as the 'bulk material' without interfaces, material scale dog bone shaped ABS bars (see Figs. 4(a), 5(a), and 6(a)) were printed in horizontal direction using an Ultimaker 2+ commercial FDM 3D printer and subjected to uniaxial tensile tests, similar to previous studies by Xu et al. [28,31]. The interface specimens are manufactured in the same manner but required somewhat larger dog bone shaped specimens in order to ensure proper and consistent printing quality, and make them manageable for testing. The intra-layer bond specimens (depicted in Figs. 4(b), 5(b), and 6(b)) were printed in horizontal direction. Lastly, the inter-layer bond specimens (shown in Figs. 4(c), 5(c), and 6(c)) were printed in vertical direction. Seeing the considerable consequences of (minor deviations in) printing settings on the material behaviour of extruded 3D printed polymers [33], these are kept constant throughout all length scales and are displayed in Table 1.

All three specimens were subjected to uniaxial tensile tests with an elongation speed of 5×10^{-3} mm s^{-1} by a Micro Tension–Compression Testing device. The resulting stress and displacement graphs are shown in Fig. 7(a-c). The determination of the constitutive relationships for each of the three phases is straightforward and follows directly from the nominal cross-sectional area of the ABS dog bones. From these figures, it can be seen that four bead phase specimens, three intra-layer bond specimens and three inter-layer bond specimens were tested successfully. Although the loads are recorded accurately, the specimens were too small for using Linear Variable Differential Transformers (LVDTs) such that the displacements are only measured from the testing device itself. The recorded displacements are therefore much larger compared to reality as the measurements include significant deformation as a result of load transmission mechanisms within the test setup. Hence, similar to Xu et al. [32], only the measured strengths (i.e. peak loads) have been taken from the experiments. The average tensile strength of the three phases are computed to be 39.8 MPa for the bead material, 21.88 MPa for the intra-layer bond, and 4.58 MPa for the inter-layer bond. These average strengths and their corresponding standard deviations (±3.78 MPa, ±1.41 MPa, and ±0.76 MPa, respectively) are depicted in Fig. 7(d). Due to the lack of stiffness information, Young's modulus was assumed to be equal to its value provided by the manufacturer (E = 1590 MPa). Poisson's ratio was taken as 0.5 based on identical assumptions. Similar to Xu et al. [32], the shear modulus, G, is computed through Eq. (4) for isotropic materials. According to the aforementioned study and references therein, even though anisotropic behaviour should be accounted for when exceeding the elastic regime (e.g. strength), the shear modulus of printed material can be assumed isotropic since printing direction has limited effect on the elastic properties:

$$G = \frac{E}{2(1+\nu)}. \tag{4}$$

From all the reviewed characterizations and models in [33], the most important ones are considered to be the geometrical analyses, since these provide valuable insights for geometrical descriptions and idealizations of 3D printed microstructures using the FDM technique. The best model for representing the microstructural morphology of

Table 1
Configurations of printing parameters.

Printing parameters	Configurations
Printing temperature (°C)	260
Printing speed (mm s^{-1})	53
Nozzle size (mm)	0.6
Layer thickness (mm)	0.15

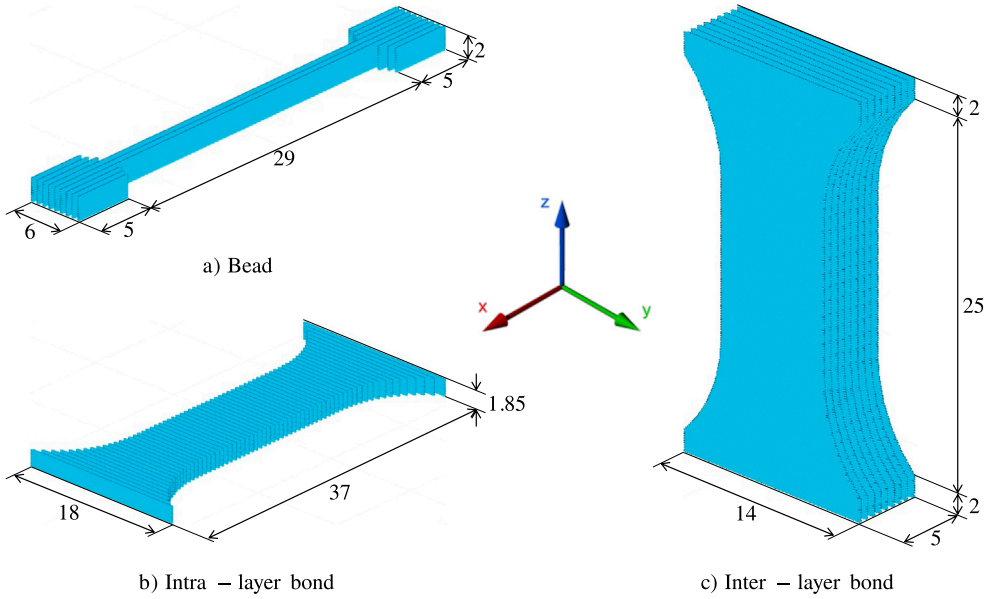

Fig. 5. G-codes of material scale dog bone shaped specimens for (a) bead, (b) intra-layer bond, and (c) inter-layer bond property determination (dimensions in mm).

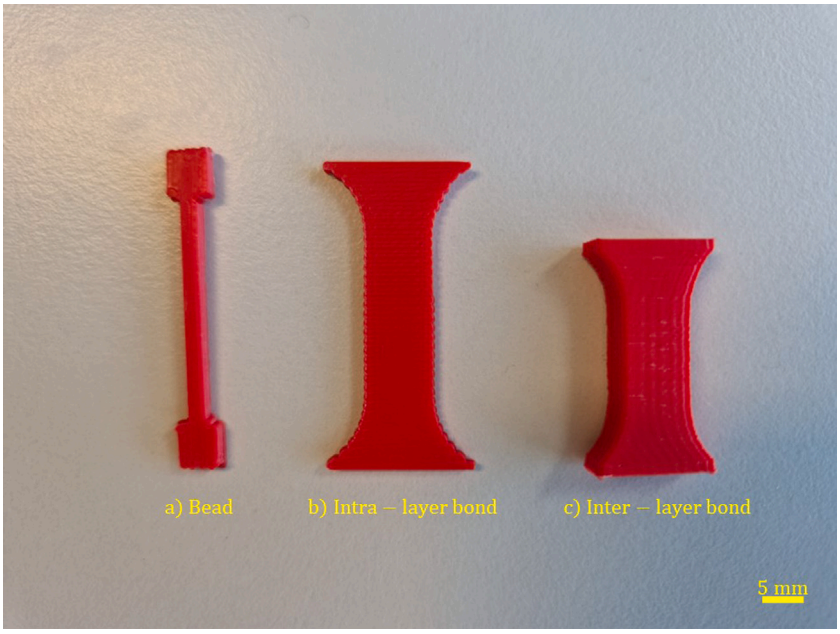

Fig. 6. Manufactured material scale dog bone shaped specimens for (a) bead, (b) intra-layer bond, and (c) inter-layer bond property determination.

FDM 3D printed polymers was found in the geometrical models by Ahn et al. [68] and its extension in [69]. Therefore, it was chosen to model the microstructures of FDM printed parts using the extended model in [69]. This model requires five input parameters: the layer thickness (t), vertical overlap interval (c), air gap (H), raster orientation (β), and cross-sectional shape parameters (a, b) or the ratio between the bead's long and short axes ($r = a/b$). However, the model has been modified and extended here by adding the layer width (L), horizontal overlap interval (d), inter-layer bond width (w_{inter}), and intra-layer bond height (h_{intra}) in view of measurements as shown in Fig. 8.

Fig. 9 depicts a sideways section of a CT scan from an ABS FDM 3D printed cubic specimen (8 × 8 × 13 mm) at a resolution of 6 µm with the same printer settings as listed in Table 1. Similar to [67], the layer thickness is controlled by squeezing the extruded filament, which is done here to enhance strength. Several measurements of the vertical and horizontal overlap intervals as well as the layer thickness and width were performed for two random locations across the scanned areas at three different specimen depths. Overall, the considered microstructures show consistent average dimensions and correspond well with the configured printer parameters in Table 1. Because the overall dimensions were found to be consistent along the depth of the part, it is assumed that the cross-sectional dimensions are constant over the entire depth. The average input parameters for the extended geometrical model shown in Fig. 8 as obtained from CT scans (Fig. 9) and calculated are listed in Table 2.

Fig. 9 and Table 2 illustrate that the printing parameters listed in Table 1 in combination with squeezing the filaments results in a very small porosity. Hence, the significant difference in (average) tensile strength in each of the three phases (i.e. bead, inter-layer bond and intra-layer bond) cannot be merely contributed to this phenomenon. The exact bond strengths as a result of this porosity can be determined using microstructural analyses in the form of the CT scan in Fig. 9.

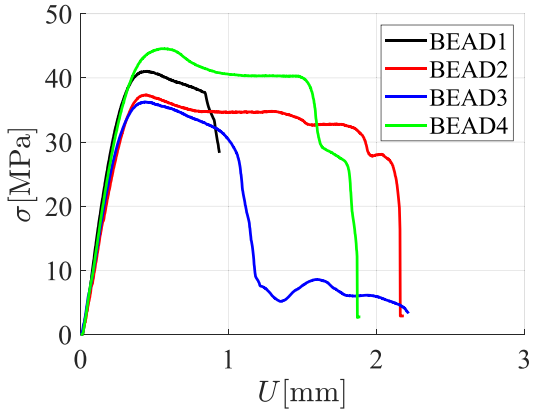

(a) Stress displacement curves of bead specimens

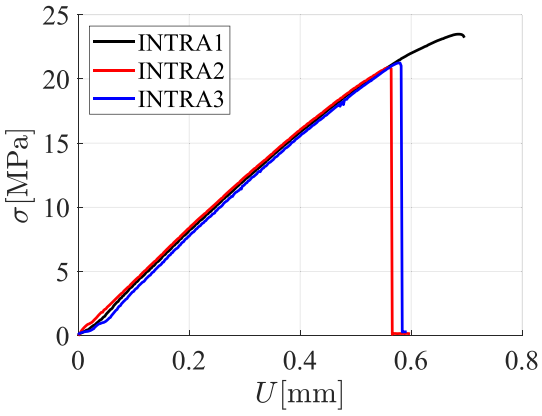

(b) Stress displacement curves of intra-layer bond specimens

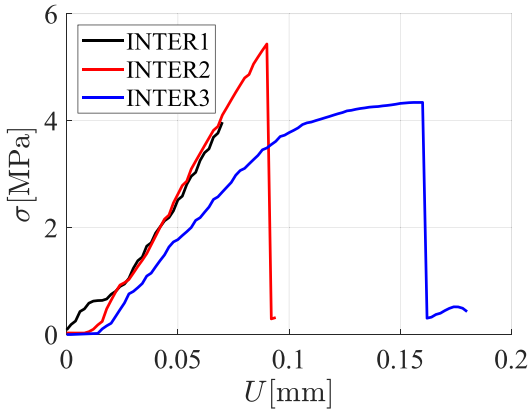

(c) Stress displacement curves of inter-layer bond specimens

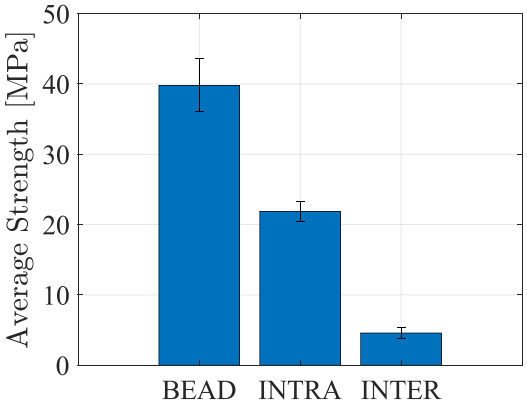

(d) Average strength values with standard deviation

Fig. 7. Representative stress displacement curves for material scale dog bone specimens.

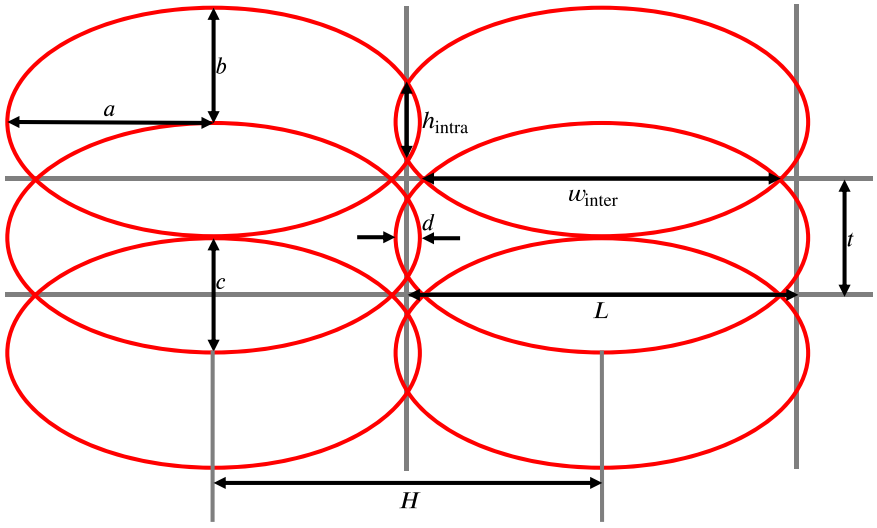

Fig. 8. Further expansion of the geometrical models by Ahn et al. [68] &[69].

Consequently, the data in Table 2 can be used to determine the actual load-bearing surface area, referred to as surface intact ratio [66,67], which is the ratio between the actual surface area of the interface (A_i) and the nominal surface area based on the bulk geometrical dimensions

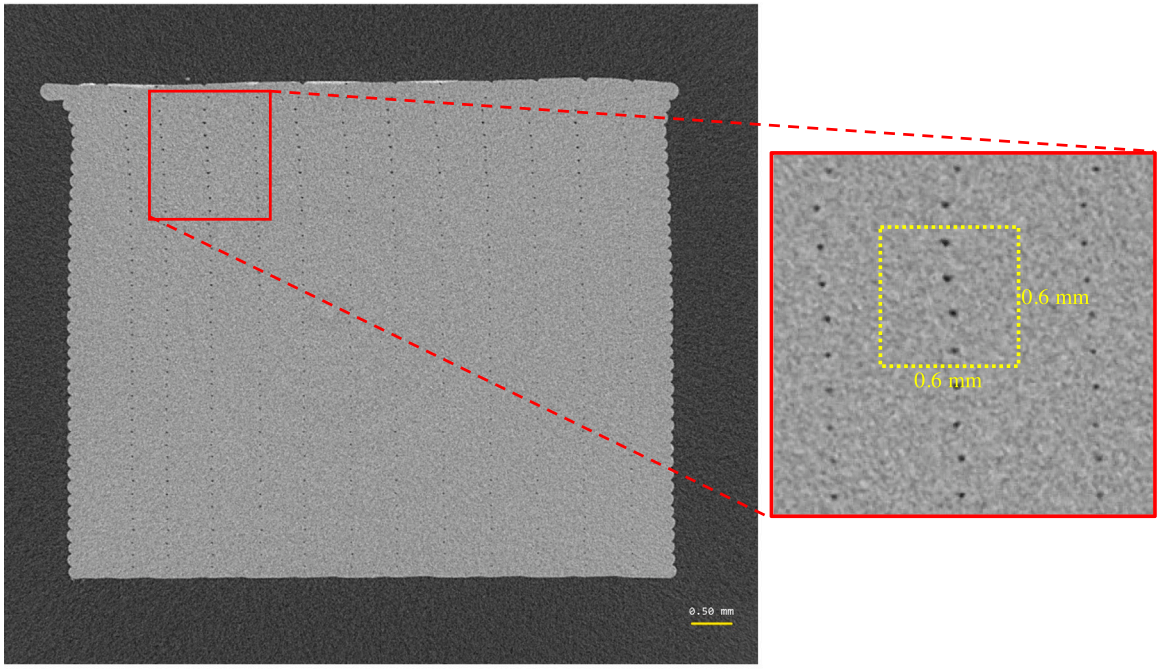

Fig. 9. Sideways section of a CT scan from an ABS FDM 3D printed part.

Table 2
Average input measurements from CT scan for extended geometrical model.

Input parameters	Dimensions (mm)	Standard deviation (mm)
a	0.3864	
b	0.1111	
c	0.0722	
d	0.1728	
h_{intra}	0.14	0.006
w_{inter}	0.57	0.027
t	0.15	0.006
L	0.6	0.027
H	0.6	0.027

(A_0):

$$r_{\text{A},i} = \frac{A_i}{A_0}\,. \tag{5}$$

In Eq. (5), A_i can be regarded as A_{intra} and A_{inter} as shown in Figs. 4(b) and (c), respectively. The above expression can be simplified for both interfaces using Fig. 8, such that $r_{\text{A,inter}} = w_{\text{inter}}/L$ and $r_{\text{A,intra}} = h_{\text{intra}}/t$. Using the average input measurements in Table 2 yields surface intact ratios equal to 0.95 and 0.93 for the inter-layer and intra-layer bonds, respectively. These reductions in cross-sectional area of the FDM 3D printed parts are much smaller compared to the actual reductions in strength measured in the experiments mentioned earlier. It can thus be concluded that only including the porosity in numerical simulations of FDM printed parts is not sufficient and that it is therefore important to *explicitly* incorporate the inter-layer and intra-layer bond properties into the numerical models developed here.

3.2. Printing path-dependent two-scale models

The experimental data in Fig. 7 clearly indicate the large anisotropy present within 3D printed parts manufactured through FDM as a result of the interfaces present in the material. Although these effects will be explicitly incorporated into the idealized microstructural RVE, their translation towards auxetic structure scale LBM analyses of the auxetic designs requires special attention. Whereas the material scale dog bone shaped specimens in Fig. 4 have straightforward and parallel printing paths, this printing process parameter becomes significantly more complex for the previously discussed planar auxetic architectures. In these more sophisticated geometries, the printing path typically follows the shape's outlines, thereby constantly changing its direction. This is illustrated in the left of Fig. 10 for the re-entrant bowtie honeycomb structure.

To explicitly incorporate the effects of both porosity and experimentally obtained interface properties into LBM simulations, the RVE will be modelled using the measured geometrical input (Table 2) and recorded constitutive relationships (Fig. 7). Because the beads are deposited in parallel, a 3D cubical RVE can be generated by extruding the cross-sectional shape of the four stacked layers with a value equal to $L = 4t = 0.6\,\text{mm}$, see the centre of Fig. 10. The constitutive relationships following from the material scale LBM simulations of this microstructural RVE should be assigned to the lattice beam elements of the FDM 3D printed auxetic structure scale models corresponding to all different printing path directions. As shown in Fig. 10, printing path directions can be straightforwardly received through the 3D printer's G-code, but the corresponding element property allocation involves additional definitions.

To facilitate the assignment of printing path-dependent properties, a local coordinate system is introduced. This coordinate system is composed of three mutually orthogonal unit vectors, n_i, s_i and t_i. The unit vector n_i is in the direction of the printing path, meaning that these are parallel (straight printing paths) or tangentially (curved printing paths) aligned. The two other unit vectors, s_i and t_i, are orthogonal and lie in the plane whose normal vector is n_i. The idealized microstructural cubical RVE of FDM 3D printed material with its direction of local coordinate axes is depicted in Fig. 10. From this convention, it can be concluded that vector s_i is always perpendicular to the platform of the FDM printer such that vector t_i, together with vector n_i, constitutes a plane that is parallel to the platform. In other words: unit vector n_i corresponds to the bead phase, vector s_i matches the inter-layer bond phase, and vector t_i reflects the intra-layer bond phase.

The printing path-dependent property assignment matches the mechanical properties for all seven adjacent directional connectivity possibilities that exist within LBM simulations. These are imposed in every local coordinate system by means of spherical angles as shown

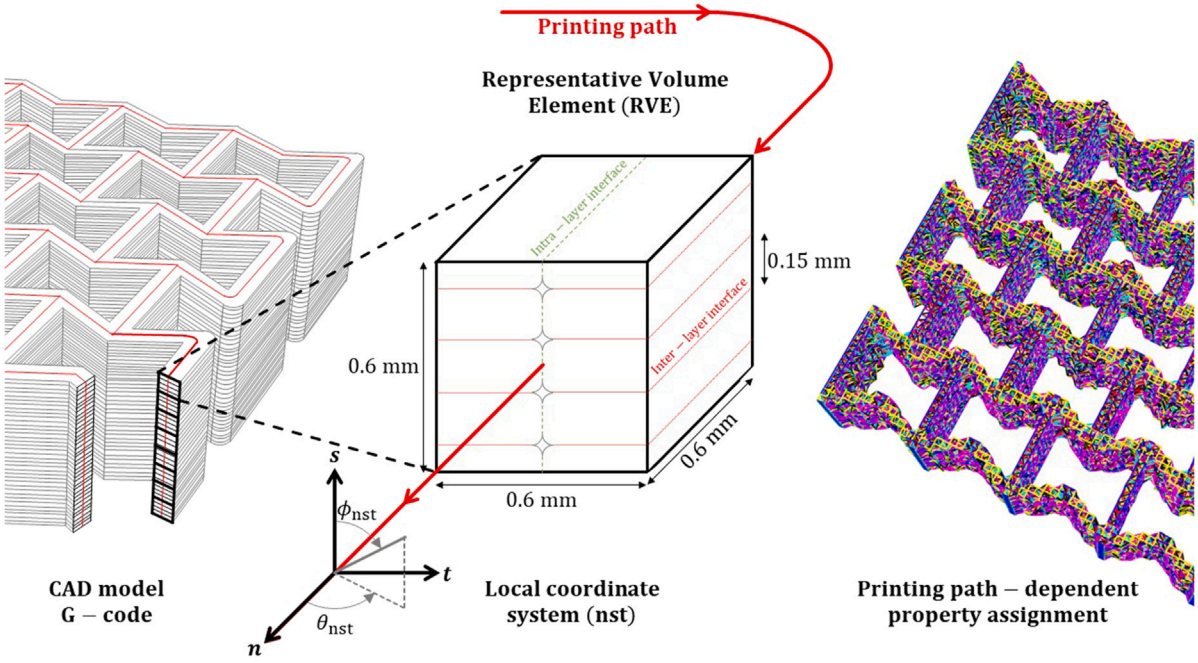

Fig. 10. Printing path-dependent two-scale model for re-entrant bowtie honeycomb structure.

Table 3
Directional element domains for printing path-dependent property assignment.

Directions	θ_{nst} (rad)	ϕ_{nst} (rad)
n	$\left[0, \frac{1}{8}\pi\right] \cup \left[\frac{7}{8}\pi, \frac{9}{8}\pi\right] \cup \left[\frac{15}{8}\pi, 2\pi\right)$	$\left[\frac{3}{8}\pi, \frac{5}{8}\pi\right]$
s	$[0, 2\pi)$	$\left[0, \frac{1}{8}\pi\right] \cup \left[\frac{7}{8}\pi, \pi\right]$
t	$\left[\frac{3}{8}\pi, \frac{5}{8}\pi\right] \cup \left[\frac{11}{8}\pi, \frac{13}{8}\pi\right]$	$\left[\frac{3}{8}\pi, \frac{5}{8}\pi\right]$
ns	$\left(0, \frac{1}{8}\pi\right) \cup \left(\frac{7}{8}\pi, \frac{9}{8}\pi\right) \cup \left(\frac{15}{8}\pi, 2\pi\right)$	$\left(\frac{1}{8}\pi, \frac{3}{8}\pi\right) \cup \left(\frac{5}{8}\pi, \frac{7}{8}\pi\right)$
st	$\left(\frac{3}{8}\pi, \frac{5}{8}\pi\right) \cup \left(\frac{11}{8}\pi, \frac{13}{8}\pi\right)$	$\left(\frac{1}{8}\pi, \frac{3}{8}\pi\right) \cup \left(\frac{5}{8}\pi, \frac{7}{8}\pi\right)$
nt	$\left(\frac{1}{8}\pi, \frac{3}{8}\pi\right) \cup \left(\frac{5}{8}\pi, \frac{7}{8}\pi\right) \cup \left(\frac{9}{8}\pi, \frac{11}{8}\pi\right) \cup \left(\frac{13}{8}\pi, \frac{15}{8}\pi\right)$	$\left(\frac{3}{8}\pi, \frac{5}{8}\pi\right)$
nst	$\left(\frac{1}{8}\pi, \frac{3}{8}\pi\right) \cup \left(\frac{5}{8}\pi, \frac{7}{8}\pi\right) \cup \left(\frac{9}{8}\pi, \frac{11}{8}\pi\right) \cup \left(\frac{13}{8}\pi, \frac{15}{8}\pi\right)$	$\left(\frac{1}{8}\pi, \frac{3}{8}\pi\right) \cup \left(\frac{5}{8}\pi, \frac{7}{8}\pi\right)$

Table 4
Directional element domains for simplified printing path-dependent property assignment.

Directions	θ_{nst} (rad)	ϕ_{nst} (rad)
n	$\left[0, \frac{1}{4}\pi\right] \cup \left[\frac{3}{4}\pi, \frac{5}{4}\pi\right] \cup \left[\frac{7}{4}\pi, 2\pi\right)$	$\left[\frac{1}{4}\pi, \frac{3}{4}\pi\right]$
s	$[0, 2\pi)$	$\left[0, \frac{1}{4}\pi\right] \cup \left[\frac{3}{4}\pi, \pi\right]$
t	$\left[\frac{1}{4}\pi, \frac{3}{4}\pi\right] \cup \left[\frac{5}{4}\pi, \frac{7}{4}\pi\right]$	$\left[\frac{1}{4}\pi, \frac{3}{4}\pi\right]$

in Fig. 10. Based on this, the directional element categories are decomposed into domains within the local coordinate system and are listed in Table 3. The implementation of the printing path-dependent property assignment is depicted in the right of Fig. 10 for the re-entrant bowtie honeycomb structure. Each colour of the lattice beam elements in Fig. 10 corresponds to a different constitutive relationship. Using the idealized microstructural RVE, a more robust and computationally affordable two-scale modelling scheme has been established for FDM 3D printed planar auxetic models which still captures the mechanical characteristics of both interfacial bond strengths due to the AM technique of material extrusion. Nevertheless, a more simplified approach has been accommodated in parallel that only considers the three main directions (n_i, s_i and t_i). The three main directions are imposed using the same local coordinate system. This coarser decomposition of directional element domains is contained in Table 4.

3.3. Calibration procedures

Simulations using LBM require calibration in terms of both the radii of the circular beam elements, as well as their strength. The beam elements' radii are iteratively determined such that the global Young's modulus of the lattice mesh is equal to the locally assigned Young's modulus for a beam element in a tensile test [52,53]. Local strength inputs are calibrated in a similar manner to ensure that the global strength matches experimental measurements. As a result, local strength inputs of LBM simulations may be somewhat different from experimentally obtained strengths, because the radii of the beam elements affect the global response. Studies on the compressive strength of 3D printed polymers are very rare [33]. Nevertheless, Vukasovic et al. [70] characterized, among others, the tensile and compressive strength of 3D printed ABS (and PLA) in two perpendicular manufacturing directions: Upright (U) where layers were extruded orthogonally to the base plate, and Flat (F) having the layers parallel to the building platform. Their results for ABS filament indicate that the strength ratio between compression and tension is affected by printing orientation. In the U direction this strength ratio equals 2, while it has a value of about 1.25 in the F direction. Because the specimens in this study are subjected to loading parallel to the building platform, the local compressive strengths in the lattice meshes representing ABS filament are assumed to be a factor 1.25 larger than the local tensile strengths calibrated from experiments. The input parameters for LBM simulations of the microstructural 3D RVE (Fig. 10) are provided in Table 5, where the subscripts correspond to the segment number of a (multi-)linear curve (see Fig. 3).

After calibration of the microstructural RVE of FDM 3D printed material in Fig. 10, its constitutive relationships can be determined to be used in the auxetic structure scale LBM analyses of the planar auxetic designs. This will be done through the use of the two-scale modelling scheme described before and the seven adjacent directional connectivity possibilities present in LBM meshes. As discussed previously, to match the mechanical properties in the planar auxetic LBM simulations with the microstructural RVE, each of the seven directions require separate constitutive relationships. The acquisition of these relationships for the three main directions is straightforward and can be obtained directly from uniaxial tensile tests along the three local

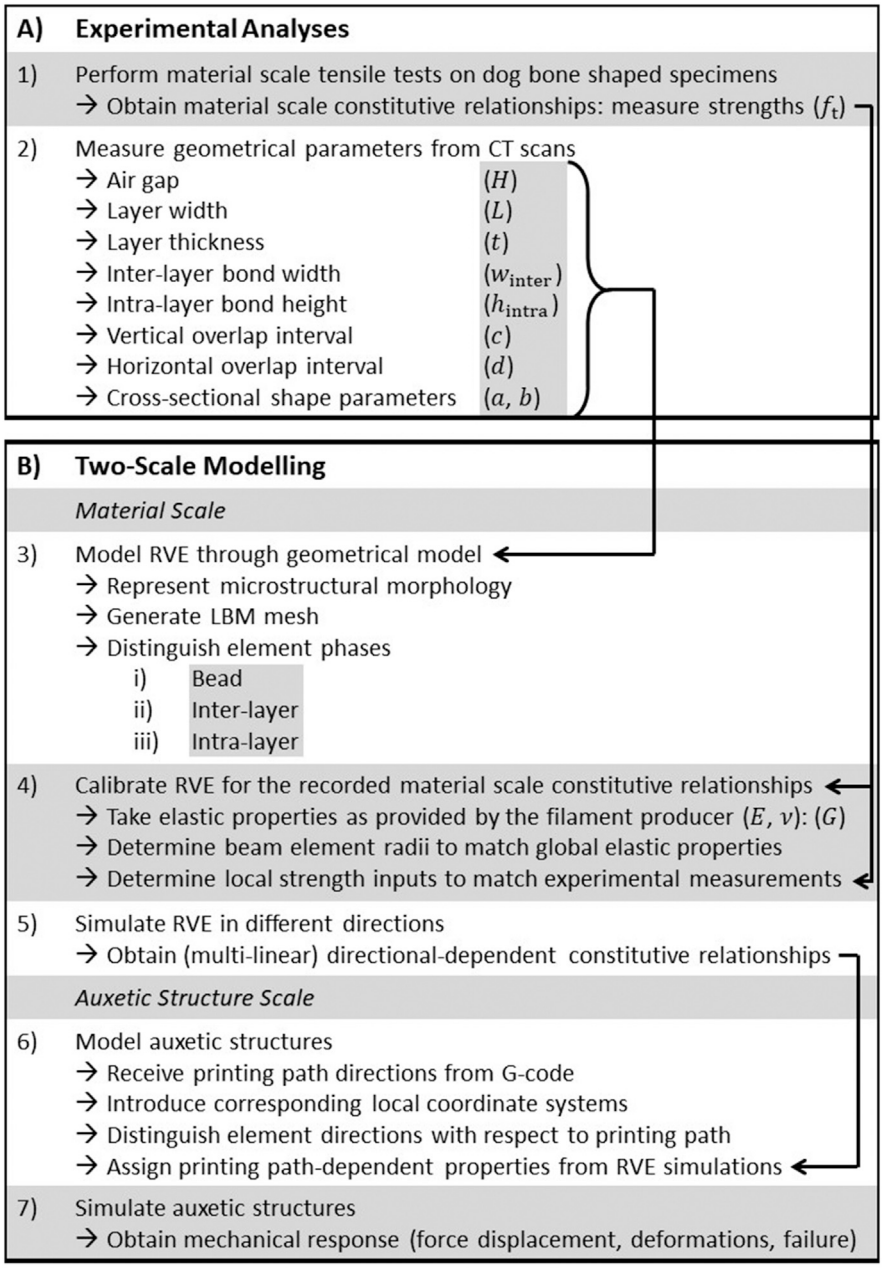

Fig. 11. Procedure for calibrating the printing path-dependent two-scale models.

Table 5
Input parameters for LBM simulations of idealized cubical RVE.

Properties (MPa)	Bead	Inter-layer	Intra-layer
E_1	1590	1590	1590
G_1	530	530	530
$f_{t,1}$	40	6.6	29
$f_{c,1}$	−50	−8.25	−36.25
E_2	343		
G_2	114.33		
$f_{t,2}$	38		
$f_{c,2}$	−47.5		

coordinate axes. However, the remaining four directions need more complicated biaxial or triaxial tensile tests.

To find the combined effect of the stress strain responses in the multi-axial tensile tests that correspond to their respective directions, stress and strain transformations are performed. The biaxial and triaxial LBM simulations only yield stresses and strains along the three main directions of the microstructural RVE, so these must be transformed in order to recompute their joint response. This will be done using *Cauchy's transformation law (principle)* [71]. Provided that θ_x, θ_y and θ_z are measured directly to the vector normal to the cut plane from their respective axes (x, y and z), the resulting normal stress may be transformed in 3D with respect to the original coordinate system as [72]:

$$\sigma_n = \boldsymbol{\sigma}_x \lambda_x^2 + \boldsymbol{\sigma}_y \lambda_y^2 + \boldsymbol{\sigma}_z \lambda_z^2 + 2(\boldsymbol{\tau}_{xy} \lambda_x \lambda_y + \boldsymbol{\tau}_{yz} \lambda_y \lambda_z + \boldsymbol{\tau}_{xz} \lambda_x \lambda_z), \tag{6}$$

where $\lambda_x = \cos(\theta_x)$, $\lambda_y = \cos(\theta_y)$ and $\lambda_z = \cos(\theta_z)$. Strain can be transformed in a similar fashion since stress and strain tensors have identical structures [71]. Therefore, using the same approach, $\boldsymbol{\sigma}$ can be simply replaced with $\boldsymbol{\epsilon}$ and $\boldsymbol{\tau}$ with $\boldsymbol{\gamma}/2$ to express the general strain transformation. Hence, computing the resulting normal strain in terms of the non-transformed strain components in the original coordinate

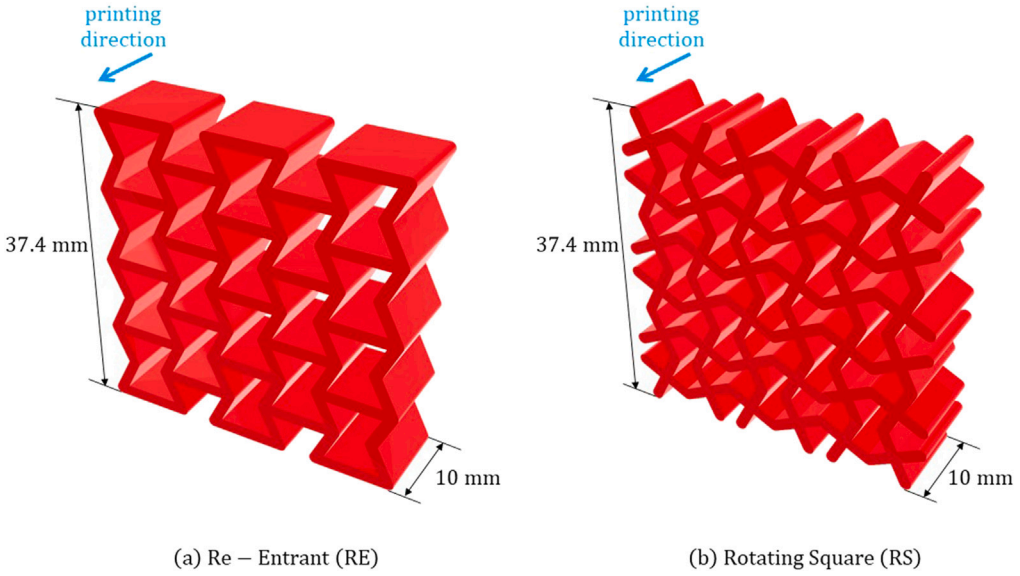

Fig. 12. Schematics of the auxetic (a) Re-Entrant (RE) and (b) Rotating Square (RS) architectures.

system as:

$$\varepsilon_n = \varepsilon_x \lambda_x^2 + \varepsilon_y \lambda_y^2 + \varepsilon_z \lambda_z^2 + \gamma_{xy} \lambda_x \lambda_y + \gamma_{yz} \lambda_y \lambda_z + \gamma_{xz} \lambda_x \lambda_z \,. \tag{7}$$

Finally, the implementation of the printing path-dependent two-scale models presented in this work is provided in Fig. 11. Starting with the microstructural experimental analysis elaborated in Section 3.1, followed by the two-scale modelling scheme described in Section 3.2 including calibration procedures for the LBM simulations in Section 3.3. It is noted once more that the given procedure requires printer settings to be kept constant throughout all length scales.

3.4. Experimental analysis of planar auxetics

To validate the two-scale approach, the auxetic structure scale LBM analyses are accompanied by experiments on planar auxetics. In view of their favourable characteristics discovered in a previous study by Xu & Šavija [31], two auxetic designs are tested in uniaxial compression: Re-Entrant (RE) and Rotating Square (RS) architectures, see Fig. 12. Both auxetic structures have similar dimensions of $37.4 \times 37.4 \times 10$ mm and are printed in the out-of-plane direction as shown in Fig. 12, which corresponds to the inter-layer direction. Identical to the microsctructural experimental analysis in Section 3.1, the RE and RS architectures were printed with the exact same ABS polymer filament and printing process parameters as listed in Table 1 to eliminate any possible influence on the results. The experimental setups for both auxetic designs are shown in Fig. 13. To reduce friction between the specimens and loading plates, a thin transparent cling film was inserted in between. In the LBM simulations of the auxetic structures, the boundary conditions are therefore assumed to be frictionless.

For each design, two specimens were subjected to uniaxial compression with a displacement rate of $0.01\,\mathrm{mm\,s^{-1}}$. The resulting load and displacement graphs are shown in Fig. 14. However, the LBM described in Section 2.1 is unable to capture self-contact or contact of initially unloaded elements with the loading plates from the experimental setup. As a result, the LBM simulations of the planar auxetic architectures are only valid up to the point where either self-contact or contact of initially unloaded elements with loading plates occurs. This will be referred to as 'validity limit' for which the comparison between the experimental results and LBM simulations holds.

The failure process of the RE specimens will be discussed first. At $u = 1.30$ mm in Fig. 15, it can be seen that failure initiates in the diagonally opposing lower left and upper right joints between the inward-facing vertical struts (circled in cyan). This event corresponds with the maximal load prior to self-contact, such that afterwards the curve starts to descend under increasing deformation. Once the aforementioned joints have failed, the RE specimen exhibits diagonal shear failure from the bottom left to the upper right corner (see cyan dashed lines at $u = 2.10$ mm in Fig. 15). Nevertheless, near a displacement of approximately 2.25 mm the diagonal pattern gets interrupted by one joint that is facing in the opposite direction (indicated by the cyan ellipse in Fig. 15). Ultimately, the RE specimens make self-contact around a displacement of 3.00 mm between the upper right struts, see the cyan ellipse in Fig. 15. This value of displacement marks the 'validity limit' of the RE design.

The RS specimens undergo more complicated deformations that arguably affect their 'validity limit'. At the onset of non-linearity (near 1 mm in Fig. 16) at least one of the exterior struts starts to fail as a result of plastic yielding, such that the specimen shows non-linear response. However, arguably the non-linearity partially comes from yielding of the ABS material itself as well. The two diagonally opposing lower left and upper right struts fail almost simultaneously before the inner structure makes contact with the bottom loading plate (see cyan ellipses at $u = 1.80$ mm in Fig. 16) such that the RS architecture started to slightly rotate counterclockwise in the experiments. It is likely that the rotation caused additional displacements and explains the presence of the first local maximum in the load and displacement graph. At this level of displacement, the interior structure of the RS specimens makes contact with the bottom loading plate. Nonetheless, at the first local minimum the RS design settles near 1.80 mm of displacement after which the curve starts ascending again. This increase in load continues until a displacement of about 2.25 mm, which approximately corresponds to the second local maximum in the force displacement curve. As shown in the photograph for $u = 2.25$ mm in Fig. 16, several occasions happen in favour of a secondary or alternative 'validity limit'. To start with, the second and third exterior upper struts from the right that are directed towards each other start to make self-contact (upper right ellipse at $u = 2.25$ mm in Fig. 16). Furthermore, the interior structure makes contact with the upper loading plate. Finally, contrary to the exterior struts, the joints between the diagonally opposing upper left and lower right inward-facing vertical struts begin to fail (circled in cyan for $u = 2.25$ mm in Fig. 16). The latter explains the small descend in the load and displacement graph, while the deformed configuration of the RS specimen is provided for 3.00 mm of displacement in Fig. 16 to illustrate that the aforementioned joints indeed fail (to such an extend

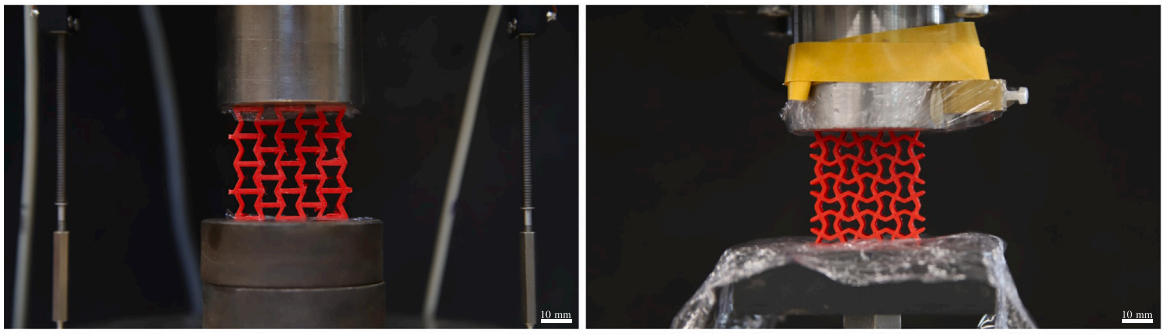

(a) Re-Entrant (RE) (b) Rotating Square (RS)

Fig. 13. Experimental setups for uniaxial compression tests of (a) Re-Entrant (RE), and (b) Rotating Square (RS) architectures.

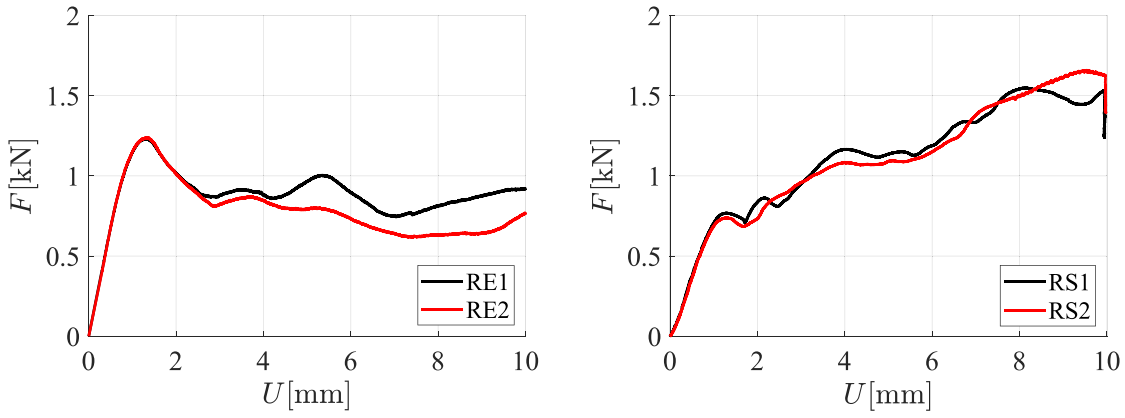

(a) Re-Entrant (RE) (b) Rotating Square (RS)

Fig. 14. Force displacement curves for uniaxial compression tests of (a) Re-Entrant (RE), and (b) Rotating Square (RS) architectures.

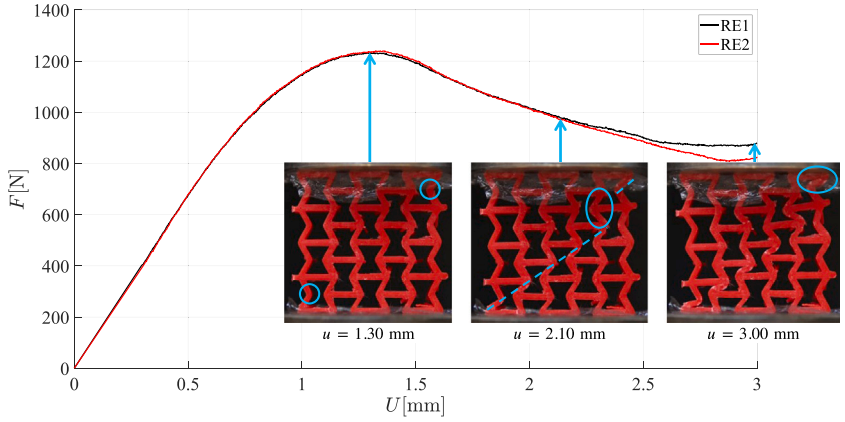

Fig. 15. Illustration of RE specimens deformation and self-contact.

that the adjacent horizontal exterior struts start to touch, see cyan circles). Hence, a displacement of $u = 2.25$ mm marks the 'validity limit' of the RS design.

Finally, two comments should be made before discussing the results. The first one is that although the 'validity limits' established here for the two planar auxetic designs seem small compared to their corresponding force displacement curves, it is important to note that the present study is only concerned with their mechanical and failure behaviour under small deformations. Modelling large deformations, including self-contact or even compaction, is beyond the scope of the current work. Moreover, this is reflected by the chosen modelling technique, LBM, of which the previously described limitations are duly noted. Therefore, with the intention of modelling small deformations and failure of planar auxetic structures, LBM simulations are very well capable of capturing their characteristic traits within its valid range. Secondly, it should be noted that discrepancies in strut widths exist among the Computer Aided Design (CAD) models and actually printed specimens. The CAD models are in agreement with the configured printer settings provided in Table 1 (i.e. nozzle size = 0.6 mm), such that the strut widths are modelled to have two neighbouring beads in each strut (i.e. $2L = 1.2$ mm). However, the strut widths measured from the actually printed specimens by means of a caliper show to be larger, having a value of 1.4 mm: a difference of nearly 17 %. The planar auxetic models used in the LBM simulations are therefore not directly obtained

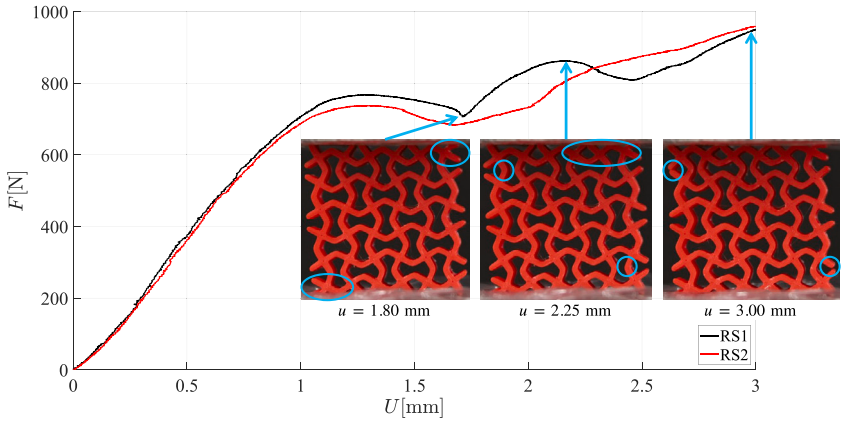

Fig. 16. Illustration of RS specimens deformation and self-contact.

from the original CAD models, but are modified according to this 17 % increase in strut width to facilitate more realistic representations.

4. Results

The results from the proposed two-scale modelling of 3D printed auxetics will be discussed here. Starting with the material scale through the idealized microstructural cubical RVE containing four stacked layers of FDM 3D printed polymer with the explicit incorporation of both porosity as well as inter-layer and intra-layer bond properties. The calibrated experimentally obtained input used for the LBM simulations of the RVE can be found in Table 5. From these microstructural simulations, constitutive relationships are determined to be used as input for the auxetic structure scale LBM analyses of the planar auxetic designs. Subsequently, printing path-dependent characteristics are allocated to the lattice beam elements of the FDM 3D printed auxetic structure models corresponding to all different printing path directions. Two different discretizations of directional element domains are considered in this study. The first one distinguishes mechanical properties for 7 RVE directions, while the other utilizes a coarser decomposition wherein only the three main directions are included. As discussed before, the considered auxetic designs are the Re-Entrant (RE) and Rotating Square (RS) architectures.

4.1. Microstructural constitutive relationships

After the calibration of the microstructural RVE of FDM 3D printed material in Fig. 10, its constitutive relationships are determined to be used in the auxetic structure scale LBM analyses of the planar auxetic designs. To match their printing path-dependent properties for all directions, each direction requires a separate constitutive relationship. These are obtained from simulated uniaxial (**n**, **s** and **t**), biaxial (**ns**, **st** and **nt**) or triaxial (**nst**) tensile tests of the microstructural RVE. The multi-axial tensile tests require stress and strain transformations, as provided in Eqs. (6) and (7), respectively. The stress strain curves resulting from the numerical simulations of the 3D RVE are provided in Figs. 17 and 18, together with their corresponding constitutive relationships that will serve as input for the auxetic structure scale models. These segmented curves determined from the microstructural RVE responses are provided in Table 6 and will serve as input for the LBM simulations of the auxetic architectures. Recall that the local strength inputs in Table 6 may be somewhat different from the experimentally obtained strengths, because the calibrated radii of the beam elements affect their strength. Young's moduli and strength values are determined from the multi-linear constitutive relationships resulting from the RVE simulations in Figs. 17 and 18. Furthermore, as described in Section 3.1, the shear moduli for all segments are computed through Eq. (4). Note that all of the seven relations are implemented in the 7 RVE directions model, whilst only those in Fig. 17 are used for the 3 main directions model. The given mesh size matching the microstructural cubical RVE dimensions (0.6 mm) required the radii of the circular beam elements of the lattice meshes to be 0.2636 mm to have a global Young's modulus of $E = 1590$ MPa as provided by the manufacturer.

Table 6
Printing path-dependent directional element properties.

Properties (MPa)	n	s	t	ns	st	nt	nst
E_1	1590	1570	1584	1912	1912	1923	2430
G_1	530	523.33	528	637.33	637.33	641	81
$f_{t,1}$	30.77	4.57	22.03	4.58	4.58	22.86	6.93
$f_{c,1}$	−38.46	−5.71	−27.54	−5.73	−5.73	−28.58	−8.66
E_2	642		980	812	789	775	1313
G_2	214		326.67	270.67	263	258.33	437.67
$f_{t,2}$	38.93		14.31	1.96	1.90	9.38	3.75
$f_{c,2}$	−48.66		−17.89	−2.45	−2.38	−11.73	−4.69
E_3	543			780	776	776	1256
G_3	181			260	258.67	258.67	418.67
$f_{t,3}$	35.18			15.39	10.74	15.26	22.06
$f_{c,3}$	−43.98			−19.24	−13.43	−19.08	−27.58
E_4	162			313	580	346	598
G_4	54			104.33	193.33	115.33	199.33
$f_{t,4}$	10.86			19.65	8.16	18.72	10.51
$f_{c,4}$	−13.58			−24.56	−10.20	−23.40	−13.14
E_5				275	90	295	514
G_5				91.67	30	98.33	171.33
$f_{t,5}$				17.49	1.28	18.43	15.28
$f_{c,5}$				−21.86	−1.60	−23.04	−19.10
E_6				82		89	211
G_6				27.33		29.67	70.33
$f_{t,6}$				5.34		6.12	19.44
$f_{c,6}$				−6.68		−7.65	−24.30
E_7							59
G_7							19.67
$f_{t,7}$							6.09
$f_{c,7}$							−7.61

4.2. Two-scale models for planar auxetic designs

Printing path-dependent properties are assigned to the lattice beam elements corresponding to all different printing path directions as illustrated in Fig. 10 for the RE design. Recall that two different directional discretizations are considered: 7 RVE directions and 3 main directions models. The former models use all of the seven constitutive relationships that are listed in Table 6, whilst the latter models merely incorporate the n_i, s_i and t_i directions.

First the deformations and failure mechanisms will be treated. The experimental load and displacement graphs (Fig. 14) as well as their corresponding 'validity limit' with respect to the LBM simulations have already been discussed in Section 3.4. For the RE and RS architectures

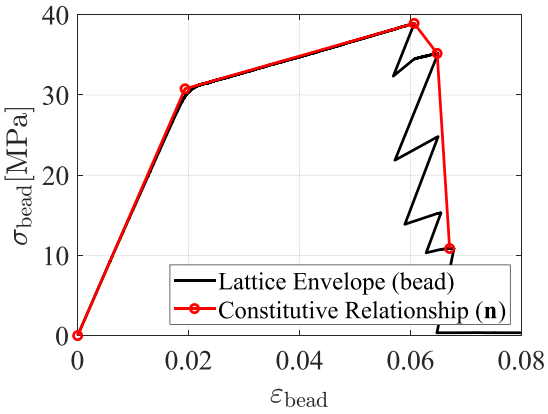

(a) Uniaxial bead or **n** direction

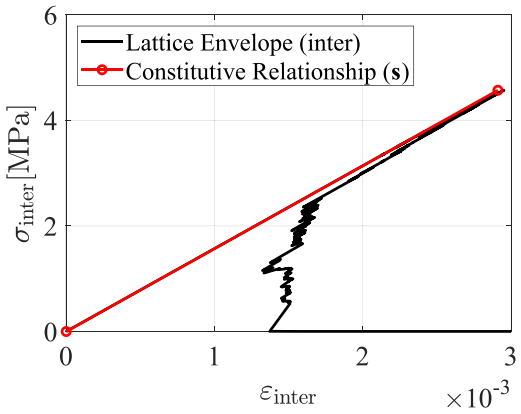

(b) Uniaxial inter-layer or **s** direction

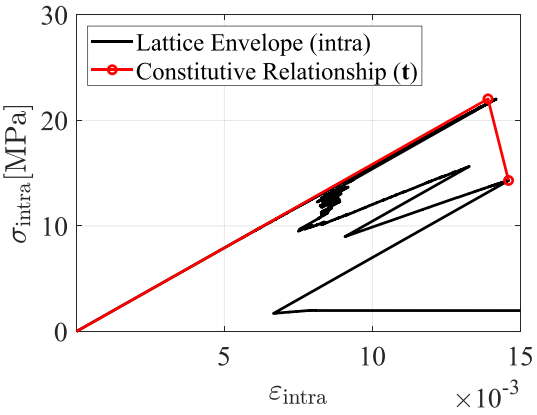

(c) Uniaxial intra-layer or **t** direction

Fig. 17. Stress strain curves from 3D RVE and their corresponding constitutive relationships for 3 main directions.

the validity limits are determined to be 3.00 mm and 2.25 mm, respectively. These particular deformations are depicted in Fig. 19, including indications of their failure mechanisms. The RE design clearly exhibits diagonal shear failure prior to self-contact (see cyan dashed lines Fig. 19(a)). In the RS design, however, first the two diagonally opposing lower and upper struts fail almost simultaneously before the interior structure makes contact with the bottom loading plate. Afterwards, as explained in Section 3.4, the second and third exterior upper struts from the right that are directed towards each other start to make self-contact and the interior structure makes contact with the upper loading plate. The final and actually considered failure mode comprises, contrary to the exterior struts, the onset of failure of the joints between the diagonally opposing upper left and lower right inward-facing vertical struts (see cyan dots in Fig. 19(b)).

As explained in Section 2.2, disorder in the lattice mesh is introduced through population of a single lattice node inside each sub-cell based on random seeds obtained from a list of generated pseudo random numbers. To see if the occurring failure mechanisms happened consistently, three numerical simulations of uniaxial compression tests are performed using different seeds for both planar auxetic designs. To this end, each auxetic cellular architecture is modelled six times: three times using different seeds for both the 7 RVE directions and 3 main directions models. The numerically obtained deformations and failure mechanisms for the RE and RS designs near their corresponding validity limits are contained in Figs. 20 and 21, respectively.

Fig. 20 showing the numerically simulated deformations and failure mechanisms of the RE architecture correspond well with the experimentally obtained phenomena in Fig. 19(a). Irrespective of the seed or discretization of directional element domains, all modelled structures show diagonal shear failure in which the inward-facing re-entrant ribs fold inwards prior to self-contact (see cyan dashed lines in Fig. 20). Nonetheless, it can be noted that the failure modes can be different depending on the element domain discretization. The computationally obtained deformations and failure mechanisms of the RS design shown in Fig. 21 are also in good agreement with the test results from Fig. 19(b). For both 7 RVE directions and 3 main directions models and all seeds, the simulated RS designs start failing at the joints between one of the inward-facing vertical struts at the bottom left (Seed = 0), upper right (Seed = 1), and bottom right (Seed = 2) as indicated by the cyan dots in Fig. 21. Directly after the failure initiation of the first joint, a second joint between the horizontally neighbouring inward-facing vertical struts fails almost simultaneously in all of the simulations — hence the double joint indications in Fig. 21. Conversely to the experimental observations, wherein first the exterior struts start to fail followed by the joints between the diagonally opposing inward-facing vertical struts, the simulated RS architectures primarily fail at the aforementioned joints after which (most of the time) at least one exterior strut fails. In Fig. 21, these later failing exterior struts are indicated by means of cyan dashed ellipses. It can thus be concluded that both failure mechanisms are captured by the numerical models, only in a different sequence. Finally, it can also be seen here that regardless of the number of considered directions (i.e. 7 or 3), the specific joints failing for the same mesh seed are consistent.

The comparison between the first eight experimentally and numerically obtained force displacement curves in Figs. 22 and 23 will be discussed next. The RS design was tested by a hydraulic press INSTRON 8872, which can directly record both the load and displacement, while the RE design was compressed by an electronic press UNITRONIC

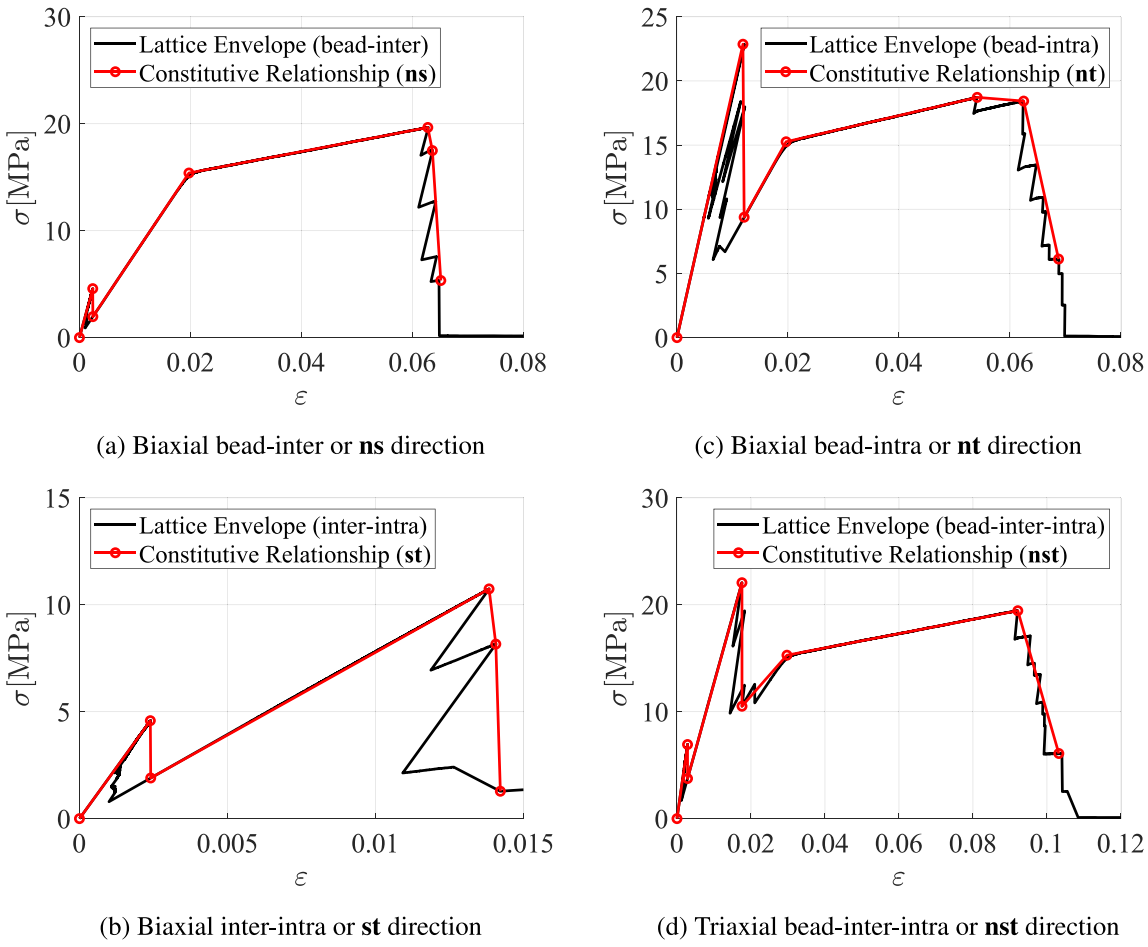

(a) Biaxial bead-inter or **ns** direction

(c) Biaxial bead-intra or **nt** direction

(b) Biaxial inter-intra or **st** direction

(d) Triaxial bead-inter-intra or **nst** direction

Fig. 18. Stress strain curves from 3D RVE and their corresponding constitutive relationships for intermediate directions.

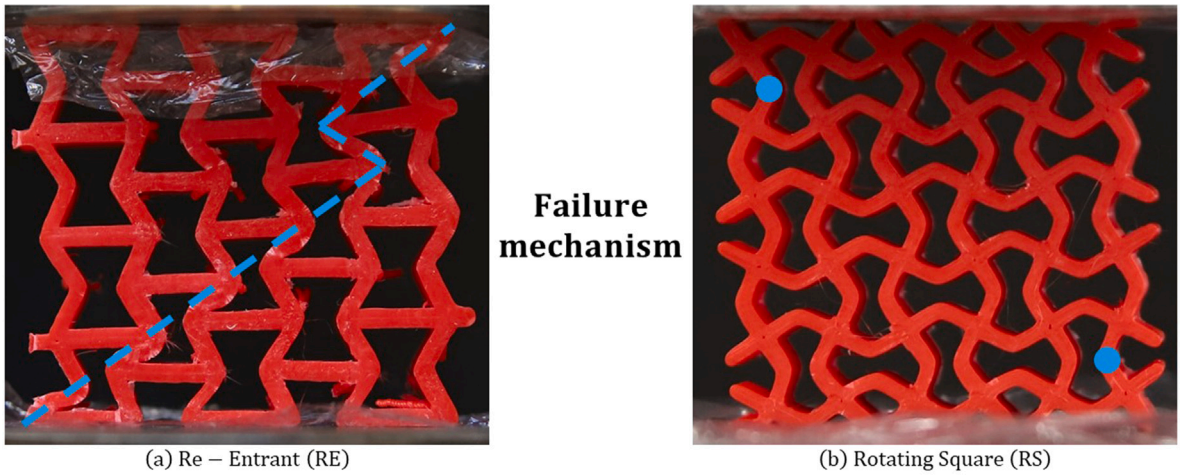

(a) Re − Entrant (RE)
$u = 3.00$ mm

(b) Rotating Square (RS)
$u = 2.25$ mm

Fig. 19. Failure mechanisms for (a) Re-Entrant (RE) and (b) Rotating Square (RS) architectures.

which requires LVDTs (as can be seen in Fig. 13(a)). The experimental results of the RE design (RE1 and RE2 in Fig. 22) are compared with their corresponding numerical counterparts (7 RVE directions, 3 main directions, and homogeneous). The stiffness of both experimental and numerical responses are very similar, with the numerical curves being slightly steeper. Furthermore, the peak loads are reached at approximately the same value of about 1200 N with percentage differences of maximally only 6 % for both directional discretization models. Also, the influence of the mesh seed shows to be marginal. The post-peak response prior to self-contact, however, is more brittle and less ductile for the simulated curves than for the test data. This is most likely caused by the nature of LBM simulations in which a stepwise element removal procedure is used. Although multi-linear constitutive relationships are used here, such that elements are not immediately removed, their stiffness and strength change in a stepwise fashion throughout the analyses. These transitions from one point on the multi-linear curve to

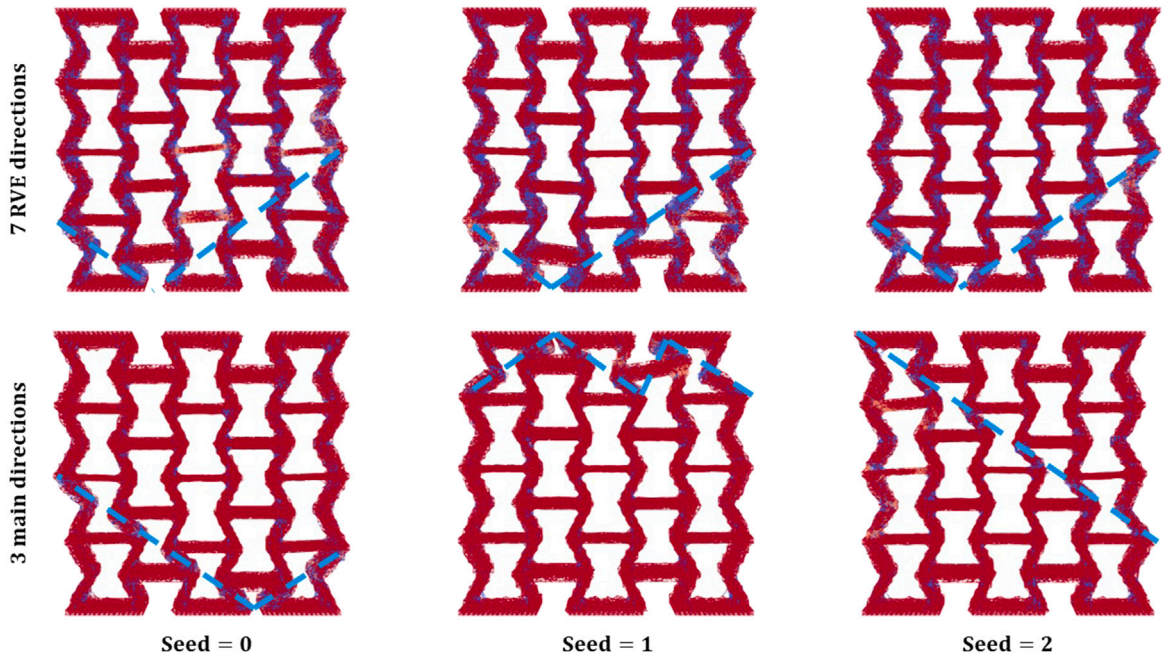

Fig. 20. Deformations and failure mechanisms of Re-Entrant (RE) architecture.

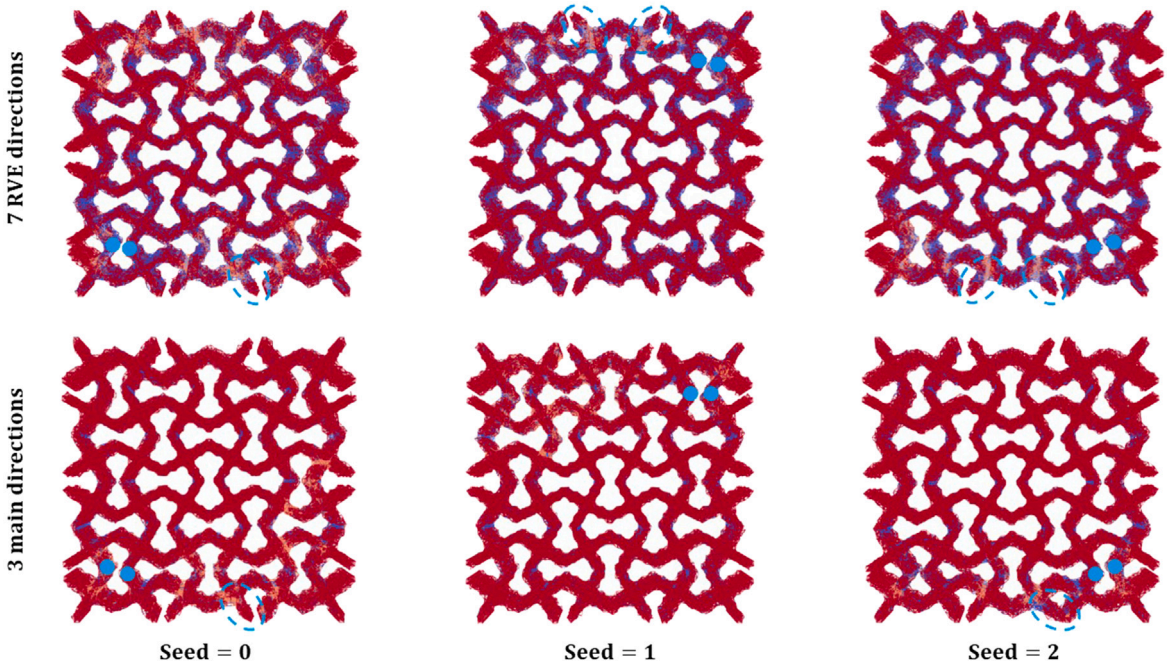

Fig. 21. Deformations and failure mechanisms of Rotating Square (RS) architecture.

the next tend to happen more rapidly and may even be accelerated through adjacent element removals near stress concentrations. As a result, the inward-facing re-entrant ribs fold inwards sooner causing the diagonal shear failure to propagate faster through the RE architecture after the onset of failure. This may also explain why in the experiments self-contact occurred only after a displacement of 3.00 mm, whereas for the simulations this already happened near 1.50 mm. Besides, there are only minor differences between the 7 RVE and 3 main directions models. The only ones worth mentioning are the fact that the stiffness of the 7 RVE directions model is somewhat larger compared to the 3 main directions model, with the slope of the former curve degenerating faster than the latter, leading to a 5 % smaller strength.

The comparison of experimental (RS1 and RS2) and first six simulated (7 RVE directions and 3 main directions) force displacement curves for the RS design in Fig. 23 will be elaborated here. In this case, the experimentally and numerically obtained stiffness are almost identical as the curves align perfectly in the initial linear-elastic stage. Only after approximately 1 mm of displacement or near 700 N do they start to deviate, that is, once both results start to behave non-linearly. It is at this very moment (1 mm displacement) that at least one exterior strut starts to fail in the experiments, such that the specimen becomes non-uniformly loaded. As a result, the RS architecture started to slightly rotate counterclockwise in the experiments. However, this may have been induced by the primary failure mode happening therein since the two diagonally opposing lower and upper struts failed almost

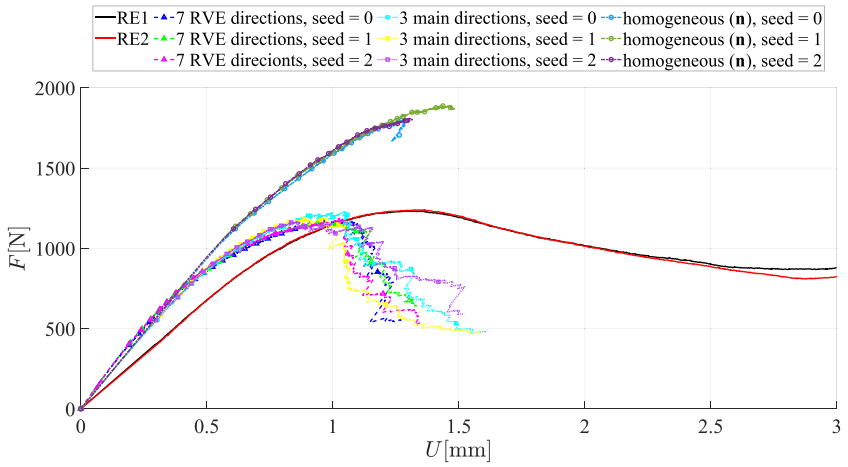

Fig. 22. Comparison of experimental, numerical and homogeneous force displacement curves for RE architecture.

simultaneously: the rotations may have enabled and caused additional displacements. As discussed before, this rotation is not captured in the deformations from the LBM simulations which is a possible explanation of their different non-linear trajectories. Because of these differences, the peak loads are reached at somewhat different displacement values: the experiments reach their maximum around 2.25 mm, while the simulations do so within 1.75 mm and 2.00 mm displacement. Nevertheless, their corresponding validity limits are reached at nearly the same deformations. Identical to the RE design simulations, the LBM simulations of the RS architecture yield approximately the same strengths compared to the experiments. Only here the difference in strength is a bit more protruding with values up to about 10 % and 12 % for the 7 RVE and 3 main directions models, respectively. Similar observations as already mentioned for the RE design can be made for the RS architecture when comparing the two different element differentiation strategy models.

Analogous to the microstructural analyses in the previous section, six additional homogeneous LBM simulations have been performed here: three different mesh seeds for each of the two planar auxetics. All elements were assigned homogeneous isotropic properties of the bead phase, in this case provided in Table 6 for the n_i direction as shown in Fig. 17(a). Be aware that the directional domain discretization is irrelevant here, as all elements are the same. The corresponding force displacement curves are plotted in Figs. 22 and 23. For the RE design the strength overestimation is more prominent when looking at the homogeneous Lattice Envelopes and the experimental curves (RE1 and RE2 in Fig. 22) having a percentage difference of roughly 52 %. The RS architecture simulation results show a smaller discrepancy among the homogeneous and heterogeneous models (30 %), even though the homogeneous curves and testing data (RS1 and RS2 in Fig. 23) deviate around 40 %. This shows once more that neglecting the anisotropic (bond) properties in numerical models for FDM 3D printed polymers results in an overestimation in strength.

Finally, using Fig. 24 the LBM deformations and failure mechanisms for the homogeneous simulations can be compared to the corresponding heterogeneous simulations. Starting with the RE auxetic architecture, the homogeneous simulations (Fig. 24) fail in a more or less similar manner as the heterogeneous ones (Fig. 19(a)) having a diagonal shear band as indicated in both figures by the cyan dashed lines. Besides, the homogeneous RE structures fail in a much more brittle manner, which is also evident from the force displacement graph in Fig. 22 where it can be seen that the validity limit for all homogeneous simulations is reached at the peak load without any descending branch. In the homogeneous representations of the RS design, the deformations and failure initiations are similar to their heterogeneous predecessors. Identical to the heterogeneous simulations, the indicated joints between one of the inward-facing vertical struts fail first for homogeneous properties too (see cyan dots in Fig. 24). Similarly, a second neighbouring joint between inward-facing vertical struts fails almost simultaneously afterwards (again, hence the double indications in Fig. 24). In contrast with the experimental observations and heterogeneous simulations, no external strut failure occurs for the homogeneous RS structures. Instead, all of the horizontally aligned joints between inward-facing vertical struts fail consecutively as indicated by the cyan dash-dotted line in Fig. 24. The latter observations are inconsistent with the experiments and heterogeneous models.

4.3. Output analysis

To understand numerically what the sensitivity of the simulated results is with respect to the interface properties, the percentage of completely failed elements so far is plotted against the analysis progress. This is only done for one of the simulated meshing seeds here, i.e. Seed = 0, because the results are very similar for other meshes. Besides, the deformations and failure mechanisms for this seed show to be most consistent for the considered directional discretizations (i.e. 7 RVE directions, 3 main directions and homogeneous). To make a fair comparison between each of these three different element differentiation strategy models, all of their evolutions over the analysis progress are discretized using the three main directions (n_i, s_i and t_i) that correspond to the intra-layer bond, inter-layer bond and bead phases, respectively. It should be noted that this representation indeed only directly reflects the 3 main directions models, but it is used for the 7 RVE directions models and homogeneous models here too since it would be arbitrary to compare the fully discretized seven directions models with models that contain no discretization at all.

Fig. 25 displays the percentage of failed elements versus the analysis progress of the RE design for the 7 RVE directions model (left column), 3 main directions model (middle column) and homogeneous model (right column). From the graphs contained therein it can be seen that both the 7 RVE directions and 3 main directions models primarily fail in tension, whereas the homogeneous model solely fails in compression. It is also clear that in the aforementioned heterogeneous models inter-layer failure is governing, while in the homogeneous model bead failure is dominant. In fact, the heterogeneous models mainly demonstrate interfacial failure with intra-layer failure being secondary. Fig. 26 has the same format, but distinction is made between elements failing in tension (upper row) and compression (lower row). These graphs emphasize the primary failure mode for the 7 RVE directions and 3 main directions models, which is tension, with no tensile failure occurring in the homogeneous model at all (hence no graph). They further illustrate that tensile failure in the heterogeneous models (almost) only happens at the inter-layer interface. This may be an indication of the initiation of delamination, or at least a prerequisite of the auxetics' out-of-plane behaviour. Additionally, Fig. 26 shows that the percentages of

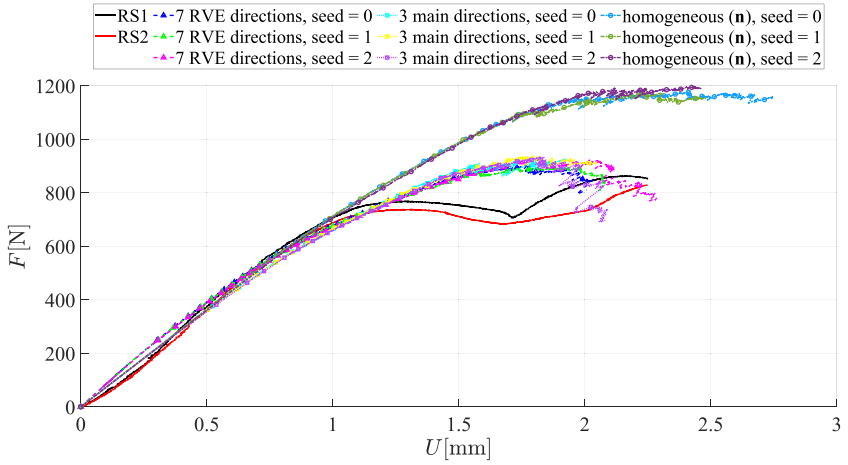

Fig. 23. Comparison of experimental, numerical and homogeneous force displacement curves for RS architecture.

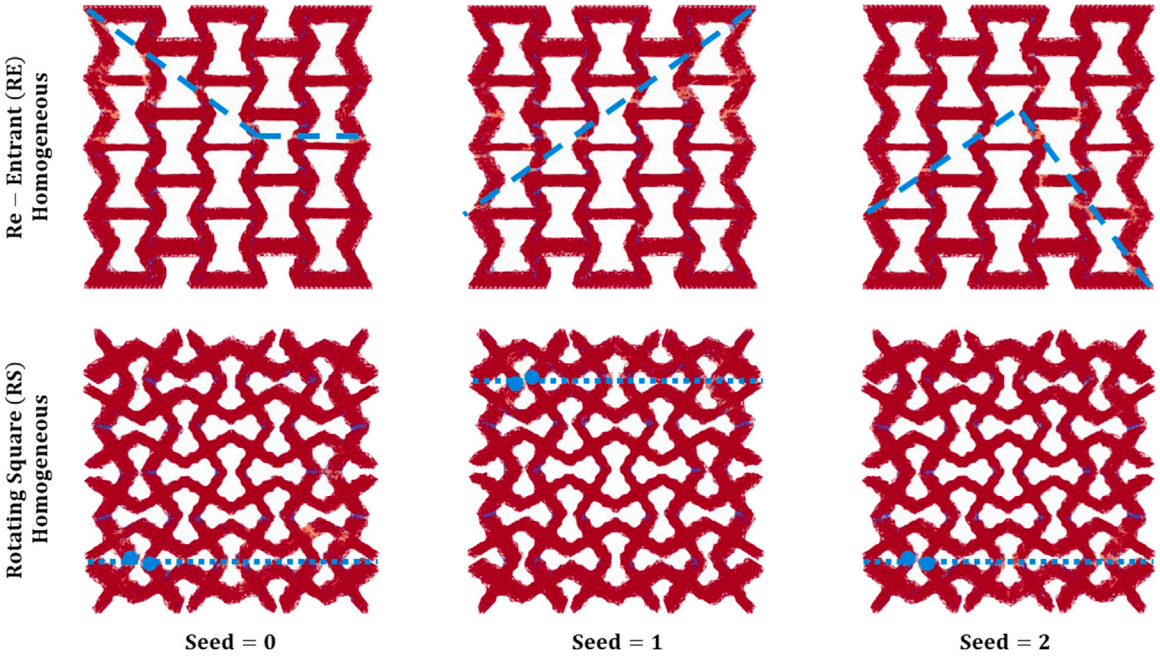

Fig. 24. Deformations and failure mechanisms for homogeneous Re-Entrant (RE) and Rotating Square (RS) architectures.

failure in tension among the 7 RVE directions and 3 main directions models are almost identical. The homogeneous model, however, only exhibits interfacial failure in a minor fraction of elements. In compression, the discretized percentages of failed elements for the 7 RVE directions model are rather close with intra-layer, inter-layer and bead failure being primary, secondary and tertiary, respectively. Nevertheless, please recall that the chosen domain discretization reflects the 3 main directions model and that in the 7 directions model there are four additional element directions having different properties (e.g. more strain capacity) that are now also partially contained in one of the three main directions, which may cause a somewhat distorted image. To conclude, no (significant) bead failure occurs in the heterogeneous models until near the end of the analysis progress whilst in the homogeneous model barely any interface failure takes place at all. This is a possible explanation of both the strength overestimation as well as the much more brittle failure happening in the homogeneous simulations. Contrary, given the absence of (significant) bead failure and the fact that a substantial fraction of interface elements initially fails in the heterogeneous simulations endorse their softening behaviour.

In Figs. 27 and 28, the percentages of failed elements against the analysis progress for the RS architecture are provided in a similar configuration. Nearly identical observations as for the RE design can be made for the RS simulations, starting with Fig. 27, the major tensile failure in the 7 RVE directions and 3 main directions models and (almost) sole compressive failure in the homogeneous model. Only here the fraction of tensile failure sticks out more compared to the RE simulations. Furthermore, the heterogeneous models primarily fail at the inter-layer bond here too, as well as the homogeneous model's dominant bead failure. A major difference for the heterogeneous models with respect to their RE counterparts is that besides the inter-layer failure, the fraction of failed elements (in either tension or compression) is much more limited and starting to develop later for the RS structures. Similar things can be concluded from Fig. 28, such as the 7 RVE directions and 3 main directions models primarily failing in tension, whilst the homogeneous simulation mainly fails in compression with only a marginal fraction of tensile failure. It is again noteworthy that the heterogeneous models in tension (almost) fail at the inter-layer bond alone. Once more, this observation is in favour of initiation of delamination of the planar auxetics. Analogous to the RE architecture, the homogeneous model of

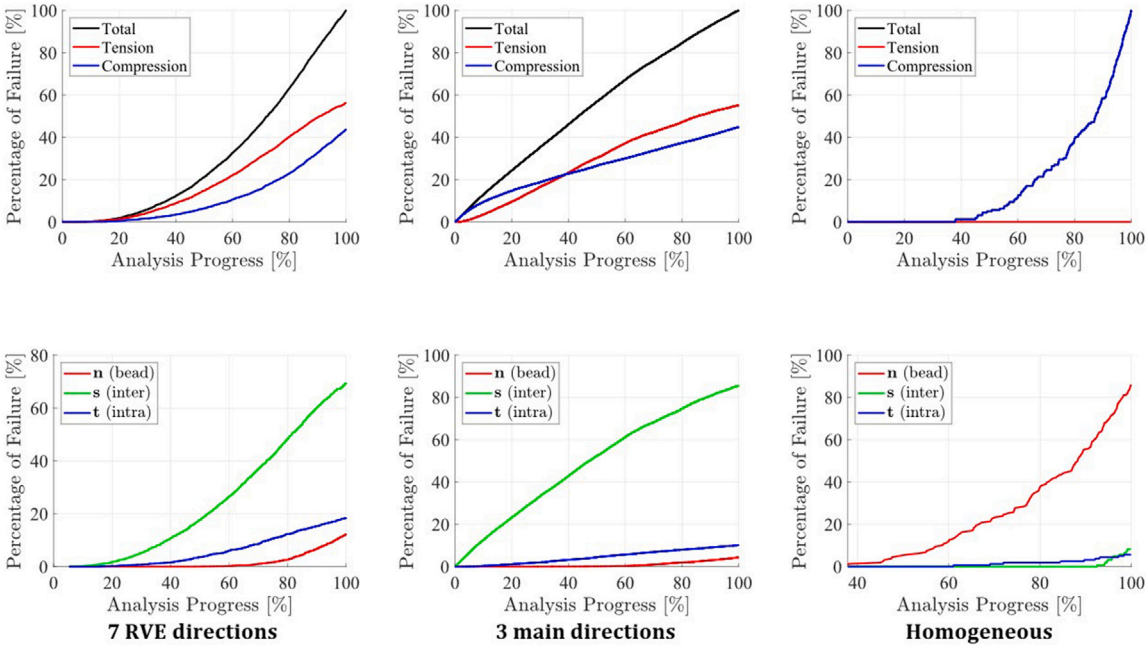

Fig. 25. Percentage of locally failed elements versus analysis progress of RE architecture.

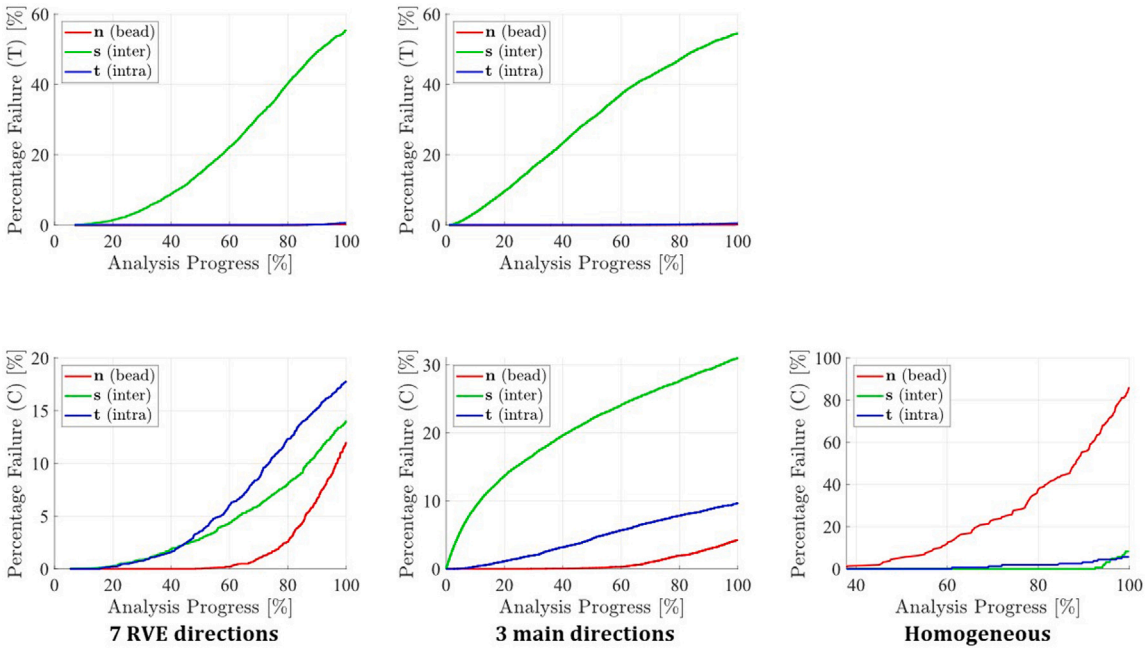

Fig. 26. Percentage of locally failed elements in Tension (T) and Compression (C) versus analysis progress of RE architecture.

the RS design experiences limited failure in the intra-layer and inter-layer bonds. Finally, similar to the RE simulations, no (significant) bead failure occurs in the heterogeneous models until near the end of the analysis progress while in the homogeneous model barely any interface failure takes place at all. These observations, together with the evidence that in the heterogeneous models there is almost no bead failure when there is a lot of interfacial failure happening, could explain the overestimation in strength for the homogeneous models.

5. Summary & conclusions

The deformation and fracture of FDM 3D printed planar auxetics have been modelled by means of the proposed two-scale modelling procedure presented in this study. First, models on the material scale from an idealized microstructural cubical RVE obtained from CT data are considered to explicitly incorporate the observed porosity and interface properties (i.e. inter-layer and intra-layer bonds). The output from this microstructural model was used as input for auxetic structure scale LBM simulations of planar auxetic designs having printing path-dependent properties. Two auxetic architectures are considered: Re-Entrant (RE) and Rotating Square (RS) designs.

Based on the results from the idealized microstructural RVE, it has been illustrated that only including the porosity in numerical simulations of FDM printed parts is not sufficient. This argument is supported by numerical results of a homogeneous RVE (including porosity), yielding higher strengths and more ductile responses than the experimentally obtained constitutive relationships. Moreover, force

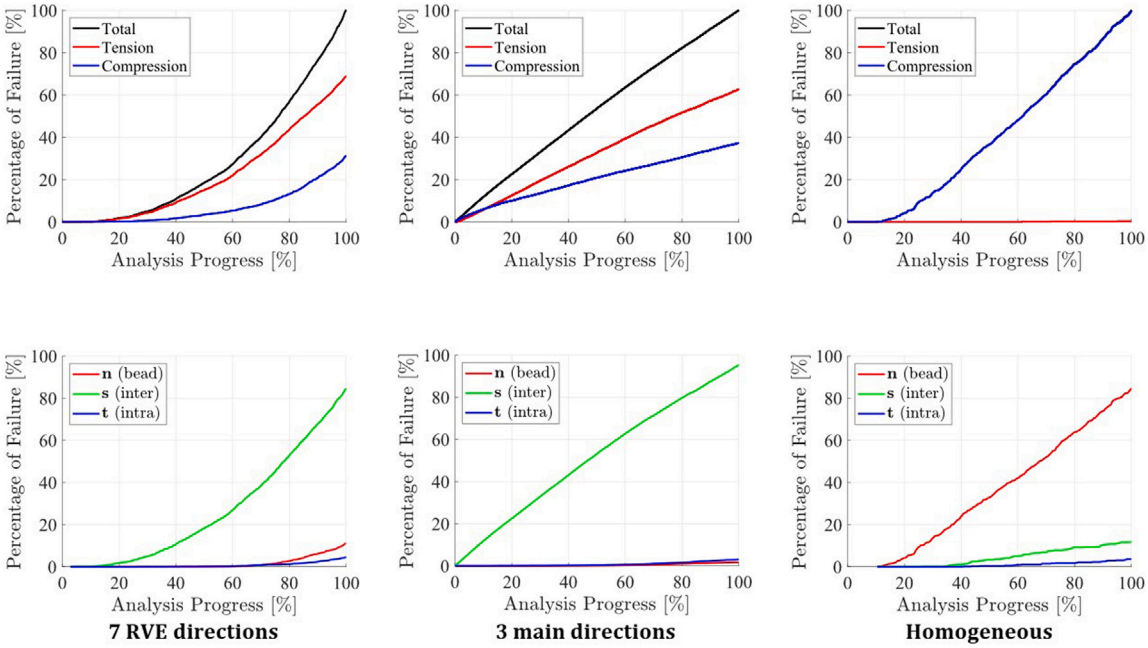

Fig. 27. Percentage of locally failed elements versus analysis progress of RS architecture.

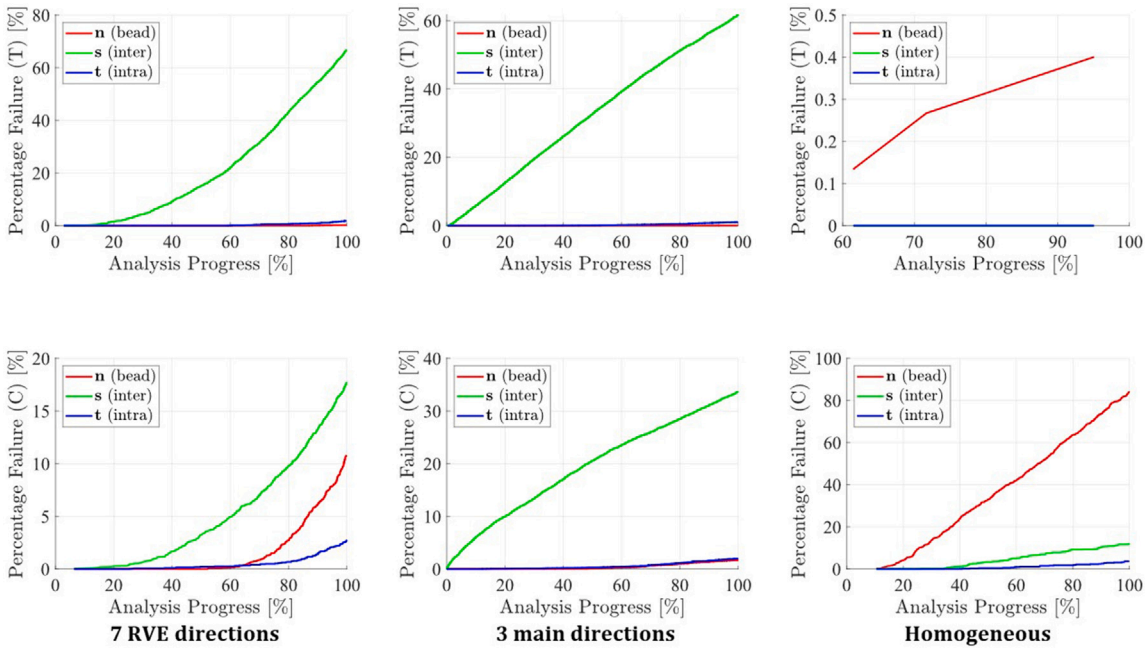

Fig. 28. Percentage of locally failed elements in Tension (T) and Compression (C) versus analysis progress of RS architecture.

displacement curves of the auxetic structure scale models of the RE and RS architectures show that neglecting the anisotropic (bond) properties in numerical models for FDM 3D printed polymers results in an overestimation in strength. The corresponding deformations and failure mechanisms (i.e. fracture) also correspond well with experimental test results. All modelled RE designs show diagonal shear failure in which the inward-facing re-entrant ribs fold inwards prior to self-contact, which is similar to experimental observations. In accordance with test recordings, the numerical RS structures all comprise failure of the joints between one of the inward-facing vertical struts and failure of one or more exterior struts touching the (virtual) loading plates. The aforementioned results hold independent of the meshing seed and directional element discretization with only minor differences between the 7 RVE directions and 3 main directions models. In terms of mechanical response, the experimentally and numerically obtained force displacement curves agree reasonably well too: the stiffness of both planar auxetic designs fit well with the experimentally measured ones while the LBM simulations generally provide a good estimation in strength with maximal percentage differences of only 6 % and 10 % to 12 % for the RE and RS architectures, respectively.

Furthermore, it has been shown on both the material and auxetic structure scales that incorporation of the interfacial bond strengths in numerical models for FDM 3D printed polymers is important. On the material scale, neglecting the weaker inter-layer and intra-layer bond properties resulted in a significantly stronger RVE response having

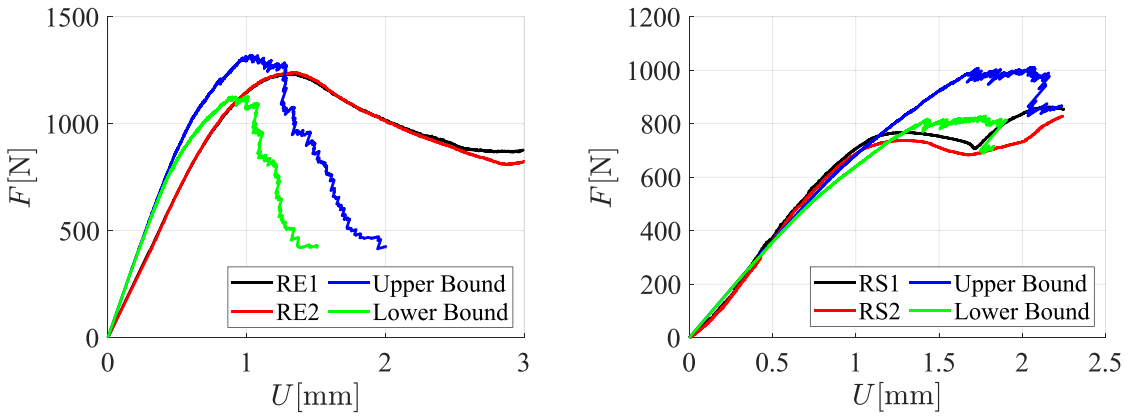

(a) Re-Entrant (RE) (b) Rotating Square (RS)

Fig. A.1. Variability influence on numerical output of (a) Re-Entrant (RE), and (b) Rotating Square (RS) architectures.

increased deformation capacity after yielding. In the auxetic structure scale models, the homogeneous isotropic material properties illustrated that neglecting the anisotropic (bond) properties provided large discrepancies between the LBM simulations and experimental measurements. Also, the obtained deformations and failure mechanisms changed when implementing homogeneous material characteristics, especially for the RS design, while the RE design exhibited a much more brittle response. The aforementioned arguments are supported by numerical investigations in which the percentage of failed elements are plotted against the analysis progress. These results clearly demonstrate that models considering interface properties primarily fail in tension, while models using homogeneous isotropic material properties mainly fail in compression. The heterogeneous models show governing failure of the inter-layer bond and that bead failure is limited until near the end of the analysis progress. In the homogeneous models, however, the majority of bead elements fail with barely any interfacial failure occurring prior to completion of the analysis.

Finally, it is important to note that the present study is only concerned with the mechanical and failure behaviour of planar auxetics under small deformations. Modelling large deformations, including self-contact or even compaction, is beyond the scope of the current study. Therefore, with the intention of modelling small deformations and failure in mind, it can be concluded that the printing path-dependent two-scale models for FDM 3D printed planar auxetics by means of LBM simulations prove to be very well capable of capturing their characteristic traits within its valid range.

CRediT authorship contribution statement

Rowin J.M. Bol: Writing – original draft, Visualization, Validation, Software, Methodology, Conceptualization. **Yading Xu:** Writing – review & editing, Resources, Investigation. **Branko Šavija:** Writing – review & editing, Supervision, Project administration, Funding acquisition, Conceptualization.

Declaration of competing interest

The authors declare the following financial interests/personal relationships which may be considered as potential competing interests: Branko Savija reports financial support was provided by European Research Council. If there are other authors, they declare that they have no known competing financial interests or personal relationships that could have appeared to influence the work reported in this paper.

Data availability

Data will be made available on request.

Acknowledgements

The corresponding author would like to sincerely thank dr. Martin Lesueur, dr. Mladena Luković and prof.dr.ir. Erik Schlangen for their valuable feedback during the evaluation of the presented research. The input, suggestions and knowledge in their respective fields of expertise really helped to improve the quality of the results contained in this work. Rowin J.M. Bol, Yading Xu & Branko Šavija acknowledge the financial support of the European Research Council (ERC) within the framework of the ERC Starting Grant Project 'Auxetic Cementitious Composites by 3D printing (ACC-3D)', Grant Agreement Number 101 041 342. The funding source was not involved in the content of this work.

Appendix

To check the influence of the variability in the material scale dog bone specimens results as shown in Fig. 7, additional auxetic structure scale simulations are carried out. For each of the two auxetic designs, RE and RS, the 3 main directions models are simulated for Seed = 0 given the following properties: all local strength inputs raised by their corresponding standard deviation values in all directions (Upper Bound in Fig. A.1), and all local strengths lowered by their corresponding standard deviation values in all directions (Lower Bound in Fig. A.1). When comparing the numerically obtained force displacement curves to the experimental results in Fig. A.1, these show upper and lower bounds for their input. The resulting load responses for RE (Fig. A.1(a)) yield percentage differences of about 6.5 % and 9.3 % for the upper and lower bounds, respectively. Similar to its comparison with the 7 RVE directions and 3 main directions models, RS returns a more protruding percentage difference around 20 % for the upper bound while the lower bound is close to only 1.8 %. Even though the force displacement output of the numerical analyses is influenced by the standard deviations in Fig. 7(d), all failure mechanisms remained the same.

References

[1] A.A. Zadpoor, Mechanical meta-materials, Mater. Horiz. 3 (2016) 371–381.
[2] M. Kadic, G.W. Milton, M.V. Hecke, M. Wegener, 3D metamaterials, Nat. Rev. Phys. 1 (2019).
[3] Y. Xu, Architected cementitious cellular materials towards auxetic behavior, 2021, Available: https://doi.org/10.4233/uuid:1a9e29a6-4868-4096-bc88-a1095cf568d3.
[4] T.C. Lim, Analogies across auxetic models based on deformation mechanism, Phys. Status Solidi - Rapid Res. Lett. 11 (2017).
[5] J.J. Warner, A.R. Gillies, H.H. Hwang, H. Zhang, R.L. Lieber, S. Chen, 3D-printed biomaterials with regional auxetic properties, J. Mech. Behav. Biomed. Mater. 76 (2017) 145–152.

[6] S. Maran, I.G. Masters, G.J. Gibbons, Additive manufacture of 3d auxetic structures by laser powder bed fusion—design influence on manufacturing accuracy and mechanical properties, Appl. Sci. (Switzerland) 10 (2020) 1–19.

[7] M.S. Rad, Y. Prawoto, Z. Ahmad, Analytical solution and finite element approach to the 3D re-entrant structures of auxetic materials, Mech. Mater. 74 (2014) 76–87.

[8] A. Joseph, V. Mahesh, D. Harursampath, On the application of additive manufacturing methods for auxetic structures: a review, Adv. Manuf. 9 (2021) 342–368.

[9] K.E. Evans, A. Alderson, Auxetic materials: Functional materials and structures from lateral thinking!, Adv. Mater. 12 (2000) 617–628.

[10] V.A. Lvov, F.S. Senatov, A.A. Stepashkin, A.A. Veveris, M.D. Pavlov, A.A. Komissarov, Low-cycle fatigue behavior of 3D-printed metallic auxetic structure, Mater. Today: Proc. 33 (2020) 1979–1983.

[11] C.-H. Hsueh, S. Schmauder, C.-S. Chen, K.K. Chawla, N. Chawla, W. Chen, Y. Kagawa, Handbook of Mechanics of Materials, Springer Nature Singapore Pte Ltd., 2019.

[12] J. Carlos, A. Elipe, A.D. Lantada, Comparative study of auxetic geometries by means of computer-aided design and engineering, Smart Mater. Struct. 21 (2012).

[13] H.M. Kolken, K. Lietaert, T. van der Sloten, B. Pouran, A. Meynen, G.V. Loock, H. Weinans, L. Scheys, A.A. Zadpoor, Mechanical performance of auxetic meta-biomaterials, J. Mech. Behav. Biomed. Mater. 104 (2020).

[14] X.T. Wang, B. Wang, X.W. Li, L. Ma, Mechanical properties of 3D re-entrant auxetic cellular structures, Int. J. Mech. Sci. 131–132 (2017) 396–407.

[15] T. Li, Y. Chen, X. Hu, Y. Li, L. Wang, Exploiting negative Poisson's ratio to design 3D-printed composites with enhanced mechanical properties, Mater. Des. 142 (2018) 247–258.

[16] Y. Xu, H. Zhang, E. Schlangen, M. Luković, B. Šavija, Cementitious cellular composites with auxetic behavior, Cem. Concr. Compos. 111 (2020).

[17] Y. Xu, E. Schlangen, M. Luković, B. Šavija, Tunable mechanical behavior of auxetic cementitious cellular composites (CCCs): Experiments and simulations, Constr. Build. Mater. 266 (2021).

[18] G.A. Lyngdoh, N.K. Kelter, S. Doner, N.M. Krishnan, S. Das, Elucidating the auxetic behavior of cementitious cellular composites using finite element analysis and interpretable machine learning, Mater. Des. 213 (2022).

[19] X. Ren, J. Shen, P. Tran, T.D. Ngo, Y.M. Xie, Auxetic nail: Design and experimental study, Compos. Struct. 184 (2018) 288–298.

[20] K.E. Evans, Auxetic polymers: a new range of materials, Endeavour 15 (1991) 170–174.

[21] R. Lakes, Foam structures with a negative Poisson's ratio, Science 235 (1987) 1038–1040, URL www.sciencemag.org.

[22] Y. Yao, L. Wang, J. Li, S. Tian, M. Zhang, Y. Fan, A novel auxetic structure based bone screw design: Tensile mechanical characterization and pullout fixation strength evaluation, Mater. Des. 188 (2020).

[23] I.G. Masters, K.E. Evans, Models for the elastic deformation of honeycombs, Compos. Struct. 35 (1996) 403–422.

[24] L.J. Gibson, Cellular solids, MRS Bull. 28 (2003) 270–274.

[25] C. Zmuda, Design of structural composite with auxetic behavior, 2017, URL http://www.wpi.edu/Academics/Projects.

[26] E. Etemadi, M. Hosseinabadi, F. Scarpa, H. Hu, Design, FDM printing, FE and theoretical analysis of auxetic structures consisting of arc-shaped and dumbell-shaped struts under quasi-static loading, Compos. Struct. 326 (2023).

[27] S. Askarinejad, H.A. Choshali, C. Flavin, N. Rahbar, Effects of tablet waviness on the mechanical response of architected multilayered materials: Modeling and experiment, Compos. Struct. 195 (2018) 118–125.

[28] Y. Xu, H. Zhang, Y. Gan, B. Šavija, Cementitious composites reinforced with 3D printed functionally graded polymeric lattice structures: Experiments and modelling, Addit. Manuf. 39 (2021).

[29] S. Qin, S. Cao, E. Yilmaz, J. Li, Influence of types and shapes of 3D printed polymeric lattice on ductility performance of cementitious backfill composites, Constr. Build. Mater. 307 (2021).

[30] C. Tang, J. Liu, W. Hao, Y. Wei, Flexural properties of 3D printed graded lattice reinforced cementitious composites using digital image correlation, Mater. Des. 227 (2023).

[31] Y. Xu, B. Šavija, Auxetic cementitious composites (ACCs) with excellent compressive ductility: Experiments and modeling, Mater. Des. 237 (2024) 112572, URL https://linkinghub.elsevier.com/retrieve/pii/S0264127523009887.

[32] Y. Xu, H. Zhang, B. Šavija, S.C. Figueiredo, E. Schlangen, Deformation and fracture of 3D printed disordered lattice materials: Experiments and modeling, Mater. Des. 162 (2019) 143–153.

[33] R.J.M. Bol, B. Šavija, Micromechanical models for FDM 3D-printed polymers: A review, Polymers 15 (2023) 4497, URL https://www.mdpi.com/2073-4360/15/23/4497.

[34] E. Monaldo, S. Marfia, Modelling of damage and plasticity phenomena in 3D printed materials via a multiscale approach, Eur. J. Mech. A Solids (2023) 105140.

[35] Z. Qian, 3D lattice analysis of cement paste, 2008.

[36] Z. Qian, Multiscale modeling of fracture processes in cementitious materials, 2012.

[37] E. Schlangen, Experimental and numerical analysis of fracture processes in concrete, 1993.

[38] A. Hrennikoff, Solution of problems of elasticity by the framework method, Appl. Mech. 12 (1941) 169–175, URL http://asmedigitalcollection.asme.org/appliedmechanics/article-pdf/8/4/A169/6744200/a169_1.pdf.

[39] B. Šavija, G.E. Smith, D. Liu, E. Schlangen, P.E. Flewitt, Modelling of deformation and fracture for a model quasi-brittle material with controlled porosity: Synthetic versus real microstructure, Eng. Fract. Mech. 205 (2019) 399–417.

[40] J.E. Bolander, S. Saito, Fracture analyses using spring networks with random geometry, Eng. Fract. Mech. 61 (1998) 569–591.

[41] M. Yip, Z. Li, B.S. Liao, J.E. Bolander, Irregular lattice models of fracture of multiphase particulate materials, Int. J. Fract. 140 (2006) 113–124.

[42] M. Sage, J. Girardot, J.B. t Kopp, S. Morel, A damaging beam-lattice model for quasi-brittle fracture, Int. J. Solids Struct. 239–240 (2022).

[43] J. Tejchman, J. Kozicki, Experimental and Theoretical Investigations of Steel-Fibrous Concrete, Springer-Verlag, Berlin, 2010.

[44] H. Zhang, Y. Xu, Y. Gan, Z. Chang, E. Schlangen, B. Šavija, Combined experimental and numerical study of uniaxial compression failure of hardened cement paste at micrometre length scale, Cem. Concr. Res. 126 (2019).

[45] M. Luković, H. Dong, B. Šavija, E. Schlangen, G. Ye, K.V. Breugel, Tailoring strain-hardening cementitious composite repair systems through numerical experimentation, Cem. Concr. Compos. 53 (2014) 200–213.

[46] N. Jiang, Z. Ge, Y. Guan, Z. Zuo, H. Zhang, Y. Ling, B. Šavija, Experimentally validated meso-scale fracture modelling of foamed concrete, Theor. Appl. Fract. Mech. 122 (2022).

[47] H. Zhang, Y. Xu, Y. Gan, Z. Chang, E. Schlangen, B. Šavija, Microstructure informed micromechanical modelling of hydrated cement paste: Techniques and challenges, Constr. Build. Mater. 251 (2020).

[48] N. Jiang, H. Zhang, Z. Chang, E. Schlangen, Z. Ge, B. Šavija, Discrete lattice fracture modelling of hydrated cement paste under uniaxial compression at micro-scale, Constr. Build. Mater. 263 (2020).

[49] D. Liu, B. Šavija, G.E. Smith, P.E. Flewitt, T. Lowe, E. Schlangen, Towards understanding the influence of porosity on mechanical and fracture behaviour of quasi-brittle materials: experiments and modelling, Int. J. Fract. 205 (2017) 57–72.

[50] B. Šavija, M. Luković, J. Pacheco, E. Schlangen, Cracking of the concrete cover due to reinforcement corrosion: A two-dimensional lattice model study, Constr. Build. Mater. 44 (2013) 626–638.

[51] Y. Xu, B. Šavija, Development of strain hardening cementitious composite (SHCC) reinforced with 3D printed polymeric reinforcement: Mechanical properties, Composites B 174 (2019).

[52] D. Gu, S. Mustafa, J. Pan, M. Luković, Reinforcement-concrete bond in discrete modeling of structural concrete, Comput.-Aided Civ. Infrastruct. Eng. (2022).

[53] S. Mustafa, S. Singh, D. Hordijk, E. Schlangen, M. Luković, Experimental and numerical investigation on the role of interface for crack-width control of hybrid SHCC concrete beams, Eng. Struct. 251 (2022).

[54] M. Lukovic, Y. Yang, E. Schlangen, D. Hordijk, On the potential of lattice type model for predicting shear capacity of reinforced concrete and SHCC structures, fib. The International Federation for Structural Concrete, 2018, pp. 804–813,

[55] Z. Chang, E. Schlangen, B. Šavija, Extended lattice model to simulate the printing process of 3D printed cementitious materials, RILEM Bookseries 28 (2020) 814–823.

[56] Z. Chang, Y. Xu, Y. Chen, Y. Gan, E. Schlangen, B. Šavija, A discrete lattice model for assessment of buildability performance of 3D-printed concrete, Comput.-Aided Civ. Infrastruct. Eng. 36 (2021) 638–655.

[57] Z. Chang, M. Liang, Y. Xu, E. Schlangen, B. Šavija, 3D concrete printing: Lattice modeling of structural failure considering damage and deformed geometry, Cem. Concr. Compos. 133 (2022).

[58] Z. Chang, H. Zhang, M. Liang, E. Schlangen, B. Šavija, Numerical simulation of elastic buckling in 3D concrete printing using the lattice model with geometric nonlinearity, Autom. Constr. 142 (2022).

[59] G. Lilliu, 3D analysis of fracture processes in concrete, 2007.

[60] Z. Chang, H. Zhang, E. Schlangen, B. Šavija, Lattice fracture model for concrete fracture revisited: Calibration and validation, Appl. Sci. (Switzerland) 10 (2020).

[61] B. Šavija, D. Liu, G. Smith, K.R. Hallam, E. Schlangen, P.E. Flewitt, Experimentally informed multi-scale modelling of mechanical properties of quasi-brittle nuclear graphite, Eng. Fract. Mech. 153 (2016) 360–377.

[62] Z. Chang, H. Zhang, E. Schlangen, B. Šavija, Z.E. Chang, Lattice model for numerical analysis of fracture process of concrete material under various loading conditions, 2019, URL https://www.researchgate.net/publication/335305423.

[63] H. Zhang, Experimentally validated multi-scale fracture modelling scheme of cementitious materials, 2019, Available: https://doi.org/10.4233/uuid:9a74f4ee-62e9-4117-bcb0-26c5a1a52cb9.

[64] A. Garg, A. Bhattacharya, An insight to the failure of FDM parts under tensile loading: finite element analysis and experimental study, Int. J. Mech. Sci. 120 (2017) 225–236.

[65] S. Sharafi, M.H. Santare, J. Gerdes, S.G. Advani, A multiscale modeling approach of the fused filament fabrication process to predict the mechanical response of 3D printed parts, Addit. Manuf. 51 (2022).

[66] N. Aliheidari, R. Tripuraneni, A. Ameli, S. Nadimpalli, Fracture resistance measurement of fused deposition modeling 3D printed polymers, Polym. Test. 60 (2017) 94–101.
[67] N. Aliheidari, J. Christ, R. Tripuraneni, S. Nadimpalli, A. Ameli, Interlayer adhesion and fracture resistance of polymers printed through melt extrusion additive manufacturing process, Mater. Des. 156 (2018) 351–361.
[68] D. Ahn, J.H. Kweon, S. Kwon, J. Song, S. Lee, Representation of surface roughness in fused deposition modeling, J. Mater. Process. Technol. 209 (2009) 5593–5600.
[69] L. Di Angelo, P. Di Stefano, A. Marzola, Surface quality prediction in FDM additive manufacturing, Int. J. Adv. Manuf. Technol. 93 (2017) 3655–3662.
[70] T. Vukasovic, J.F. Vivanco, D. Celentano, C. García-Herrera, Characterization of the mechanical response of thermoplastic parts fabricated with 3D printing, Int. J. Adv. Manuf. Technol. 104 (2019) 4207–4218.
[71] B. Aadnøy, R. Looyeh, Stress and strain transformation, 2011, pp. 13–25.
[72] M. Swanbom, 3D stress transformation and principal stresses | derivation & example using casio fx-115es plus, 2018, URL https://www.youtube.com/watch?v=YNrhKOsdDlI.